

# Thermodynamic properties of an $S = 1/2$ ring-exchange model on the triangular lattice

Kazuhiro Seki<sup>1</sup> and Seiji Yunoki<sup>1,2,3</sup>

<sup>1</sup>Computational Quantum Matter Research Team, RIKEN,  
Center for Emergent Matter Science (CEMS), Saitama 351-0198, Japan

<sup>2</sup>Computational Condensed Matter Physics Laboratory,  
RIKEN Cluster for Pioneering Research (CPR), Saitama 351-0198, Japan

<sup>3</sup>Computational Materials Science Research Team, RIKEN Center for Computational Science (R-CCS), Hyogo 650-0047, Japan

(Dated: April 30, 2022)

By using a numerically exact diagonalization technique and a block-extended version of the finite-temperature Lanczos method, we study thermodynamic properties of an  $S = 1/2$  Heisenberg model on the triangular lattice with an antiferromagnetic nearest-neighbor interaction  $J$  and a four-spin ring-exchange interaction  $J_c$ . Calculations are performed on small clusters under the periodic-boundary conditions. In contrast to the purely triangular case with  $J_c = 0$ , the specific heat exhibits a characteristic double-peak structure for  $J_c/J \gtrsim 0.04$ . From the calculation of the entropy and the uniform magnetic susceptibility, it is shown that non-magnetic excitations exist below the magnetic excitation for  $J_c/J \gtrsim 0.04$ .

## I. INTRODUCTION

The  $S = 1/2$  Heisenberg antiferromagnet on the triangular lattice is a prototypical frustrated quantum system and has been a candidate of a resonating-valence-bond (RVB) or a spin-liquid ground state [1, 2]. Although the ground state is likely to be the conventional  $120^\circ$  Néel state according to the recent numerical and theoretical studies [3–8], the quest for a spin-liquid state in the same lattice is still continuing by incorporating additional terms to stabilize a spin-liquid state, such as the next-nearest-neighbor exchange interaction [9–13] and the four-spin ring-exchange interaction  $J_c$  [14, 15]. These exchange interactions can be considered as an introduction of the charge fluctuation [16, 17] and thus become more relevant for describing magnetic properties of Mott insulators in proximity of the metal-insulator transition [18–27]. While the ring-exchange interaction itself has long been considered for describing the magnetism in the three-dimensional solid  $^3\text{He}$  [28–34],  $\text{NiS}_2$  [35], and the parent compounds of high- $T_c$  cuprate superconductor such as  $\text{La}_2\text{CuO}_4$  [36–41], its importance in triangular-lattice systems near Mott transition is attracting a renewed attention recently [14, 15, 42, 43] in organic Mott insulators  $\kappa$ -( $\text{ET}$ ) $_2\text{Cu}_2(\text{CN})_3$  [44–46] and  $\text{EtMe}_3\text{Sb}[\text{Pd}(\text{dmit})_2]_2$  [47, 48], and a charge-density-wave Mott insulator  $1T$ -TaS $_2$  [49, 50].

As an effective model for the triangular-lattice materials near Mott transition but with frozen charge degrees of freedom, the ring-exchange model on the triangular lattice has been proposed [14, 15, 42, 43]. The model is described by the following Hamiltonian:

$$\hat{H} = J \sum_{\langle ij \rangle} \hat{\mathbf{S}}_i \cdot \hat{\mathbf{S}}_j + J_c \sum_{\langle ijkl \rangle} (\hat{P}_{ijkl} + \hat{P}_{ijkl}^\dagger), \quad (1)$$

where  $J$  is the nearest-neighbor exchange coupling,  $J_c$  is the four-spin ring-exchange coupling,  $\hat{\mathbf{S}}_i = (\hat{S}_i^x, \hat{S}_i^y, \hat{S}_i^z)$  is the  $S = 1/2$  spin operator, and  $\hat{P}_{ijkl}$  permutes four spins at sites  $i, j, k$ , and  $l$  on an elementary parallelogram cyclically connected as  $i$ - $j$ - $k$ - $l$ - $i$  (see Fig. 1). More specifically, we define that  $i$ - $k$  and  $j$ - $l$  are diagonals of the parallelogram, and  $k$  is the next-nearest neighbor of  $i$  on the triangular lattice, as indicated

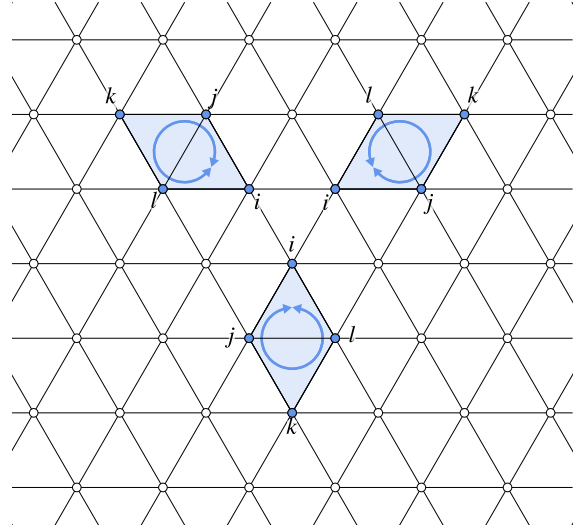


FIG. 1. Schematic of the model described in Eq. (1) on the triangular lattice. Elementary parallelograms, where  $\hat{P}_{ijkl}$  and  $\hat{P}_{ijkl}^\dagger$  act (indicated by circular arrows), are indicated.

in Fig. 1. The ring-exchange operator  $\hat{P}_{ijkl}$  can be expressed by a product of permutation operators as

$$\hat{P}_{ijkl} = \hat{P}_{il}\hat{P}_{ik}\hat{P}_{ij}, \quad (2)$$

where  $\hat{P}_{ij} = \hat{P}_{ij}^\dagger = 2\hat{\mathbf{S}}_i \cdot \hat{\mathbf{S}}_j + \frac{1}{2}$  is the permutation operator exchanging spins at site  $i$  and  $j$ . It follows that  $\hat{P}_{ijkl}^\dagger = \hat{P}_{lkji} = \hat{P}_{ijkl}^{-1}$ . The sum indicated by  $\langle ij \rangle$  in the first term of  $\hat{H}$  runs over all pairs of nearest-neighbor sites  $i$  and  $j$ , and the second sum indicated by  $\langle ijkl \rangle$  runs over all elementary parallelograms (denoted by shaded blue in Fig. 1) formed by sites  $i, j, k$ , and  $l$ .

In terms of the  $t/U$  expansion of the half-filled Hubbard model with the nearest-neighbor hopping  $t$  and the on-site interaction  $U$ , the ring-exchange term appears in the fourth-order expansion with  $J_c = 20t^4/U^3$ , although additional cor-

rection terms appear in the expansion with the fourth order [16, 17]. Note that the Hamiltonian in Eq. (1) has been considered as a model for the nuclear magnetism of a  $^3\text{He}$  film adsorbed on graphite preplated with  $^4\text{He}$  at a particular commensurate density but with a ferromagnetic  $J < 0$  [5, 51–60], although a recent fixed-node diffusion Monte Carlo calculation poses a question on the realization of such a commensurate crystalline state [61].

Since  $J > 0$  and  $J_c \geq 0$  are relevant for the magnetism near Mott transition, let us briefly summarize the ground-state phase diagram of the model in Eq. (1) for  $J > 0$  and  $J_c \geq 0$  discussed in the previous literature. For  $J > 0$  and  $J_c = 0$ , the ground state is the three-sublattice ( $120^\circ$ ) state [3–8, 14]. For  $J = 0$  and  $J_c > 0$ , the ground state is a spin-liquid state (SL-I), which corresponds to the RVB state, with no spin gap [5, 59, 62]. Another spin-liquid state (SL-II) appears for moderate  $J_c/J$  [5, 14, 59, 62], where SL-II phase has many singlet excitations in the spin gap (i.e., below the lowest magnetic excitation).

Besides exploring the spin-liquid ground states, it is also crucial to study excitation properties such as thermodynamics as they can be measured experimentally [46, 63–65]. In this paper, we examine the effect of the ring-exchange interaction on the thermodynamic properties such as the specific heat, entropy, uniform magnetic susceptibility, and generalized Wilson ratio. Recently, these thermodynamic properties, except for the specific heat, of the same model on a 28-site cluster has been reported [66] using the finite-temperature Lanczos method [67–69]. Here, we propose an extended version of the finite-temperature Lanczos method with the block Lanczos algorithm, and adopt it for small-cluster calculations up to 36 sites. The block-Lanczos extension allows for an efficient sampling over random states that is required for approximate evaluation of the trace over a basis set of the Hilbert space.

The rest of this paper is organized as follows. The finite-temperature Lanczos method with the extension to the block-Lanczos algorithm is described in Sec. II. The method is applied in Sec. III to calculate the entropy, the specific heat, the uniform magnetic susceptibility, and the generalized Wilson ratio of the model for various values of  $J_c/J$ . The results are summarized and discussed in Sec. IV. An algorithm to find a spin configuration from a given state label in a Hilbert space of a fixed magnetization  $S^z = \sum_i S_i^z$  is described in Appendix A. The effect of the ring-exchange interaction  $J_c$  on the spin-wave excitation in the  $120^\circ$  Néel state is studied within the linear spin-wave theory in Appendix B. Throughout the paper, we set  $\hbar = k_B = 1$ .

## II. METHOD

In this section, we describe the finite-temperature Lanczos method, which allows us to evaluate the partition function and thermal averages of physical observables approximately, without full numerical diagonalization of the Hamiltonian. Before entering the details, let us first briefly summarize the procedure of the finite-temperature Lanczos method. The key approximations made in the finite-temperature Lanczos

method are (i) stochastic evaluation of the trace of operator  $\hat{O}$  and (ii) approximate evaluation of Boltzmann factor  $e^{-\beta\hat{H}}$  by the Lanczos method, where  $\beta$  is the inverse temperature. We use the random-phase states for stochastic samplings in (i) and adopt the block Lanczos method for (ii).

### A. Exact partition function

The partition function  $Z$  at temperature  $T = 1/\beta$  is defined by

$$Z = \text{Tr} [e^{-\beta\hat{H}}] = \sum_{n=1}^{N_{\text{st}}} e^{-\beta E_n}, \quad (3)$$

where  $E_n$  is an eigenvalue of  $\hat{H}$  associated with an eigenstate  $|E_n\rangle$ , i.e.,

$$\hat{H}|E_n\rangle = E_n|E_n\rangle, \quad (4)$$

and  $N_{\text{st}}$  is the number of eigenstates. The thermal average of operator  $\hat{A}$  is given by

$$\langle \hat{A} \rangle = \frac{1}{Z} \text{Tr} [e^{-\beta\hat{H}} \hat{A}] = \frac{1}{Z} \text{Tr} [e^{-\beta\hat{H}/2} \hat{A} e^{-\beta\hat{H}/2}]. \quad (5)$$

In practice, one can make use of symmetries of the Hamiltonian to reduce the computational cost for numerical diagonalization or Lanczos iterations as

$$Z = \sum_{\alpha=1}^{N_{\text{sym}}} Z^{(\alpha)} \quad (6)$$

with

$$Z^{(\alpha)} = \sum_{n=1}^{N_{\text{st}}^{(\alpha)}} e^{-\beta E_n^{(\alpha)}} \quad (7)$$

and

$$\hat{H}^{(\alpha)}|E_n^{(\alpha)}\rangle = E_n^{(\alpha)}|E_n^{(\alpha)}\rangle, \quad (8)$$

where  $\alpha$  labels symmetry sectors of the Hamiltonian,  $N_{\text{sym}}$  is the number of symmetry sectors,  $N_{\text{st}}^{(\alpha)}$  is the number of states in a given symmetry sector  $\alpha$  satisfying  $N_{\text{st}} = \sum_{\alpha=1}^{N_{\text{sym}}} N_{\text{st}}^{(\alpha)}$ , and  $\hat{H}^{(\alpha)}$  is the block-diagonalized Hamiltonian, i.e.,  $\hat{H} = \bigoplus_{\alpha=1}^{N_{\text{sym}}} \hat{H}^{(\alpha)}$ .

We consider the Hamiltonian in Eq. (1) on small clusters under the periodic-boundary conditions. The symmetry sectors are labeled as  $(\alpha) = (\mathbf{k}, S^z)$ , where  $\mathbf{k}$  is the momentum and  $S^z$  is the eigenvalue of  $\hat{S}^z = \sum_{i=1}^L \hat{S}_i^z$ , and  $L$  is the number of sites. This labeling of the symmetry sectors results in  $N_{\text{sym}} = L(L+1)$ . Figure 2 shows the available momenta for the  $L = 6 \times 6$  cluster, which is the largest size used in the present study. In Appendix A, we describe an algorithm to find a spin configuration for a given state label in the fixed-magnetization Hilbert space.

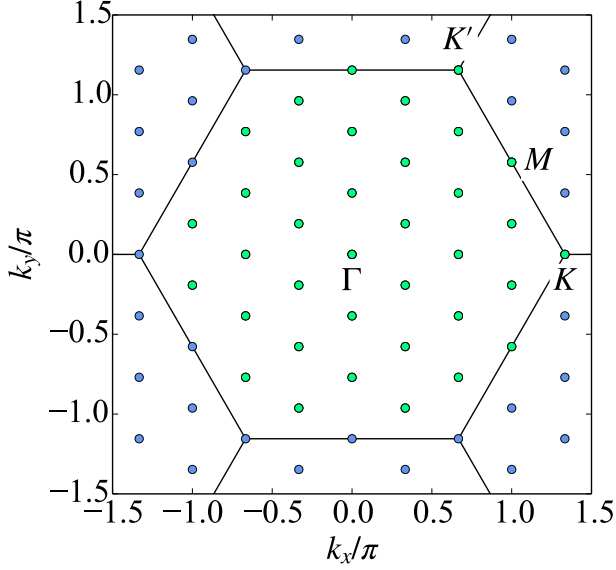


FIG. 2. Available momenta  $\mathbf{k} = (k_x, k_y)$  for the  $L = 6 \times 6$  cluster under periodic boundary conditions. Solid lines denote the Brillouin-zone boundaries and light green circles indicate the 36 momenta inside the first Brillouin zone. High symmetric momenta,  $\Gamma: (0, 0)$ ,  $K: (4\pi/3, 0)$ ,  $M: (\pi, \pi/\sqrt{3})$ , and  $K': (2\pi/3, 2\pi/\sqrt{3})$ , are also indicated.

We evaluate  $Z^{(\alpha)}$  numerically exactly if  $N_{\text{st}}^{(\alpha)} \leq 10^4$ . For evaluation of  $Z^{(\alpha)}$  with larger  $N_{\text{st}}^{(\alpha)}$ , we employ the finite-temperature Lanczos method [67–69] combined with the block-Lanczos algorithm described in the following sections. Below we drop the superscript  $(\alpha)$  labeling the symmetry sectors for brevity.

### B. Random-phase state

Following Refs. [70, 71], here we review some properties of the random-phase states, which is relevant to the stochastic evaluation of the trace. Consider a state  $|r\rangle$  such that

$$|r\rangle = \sum_{x=1}^{N_{\text{st}}} e^{i\theta_x^r} |x\rangle, \quad (9)$$

where  $\{|x\rangle\}$  is an arbitrary complete orthonormal set satisfying  $\hat{1} = \sum_{x=1}^{N_{\text{st}}} |x\rangle\langle x|$  and  $\langle x|x'\rangle = \delta_{xx'}$ , and  $\theta_x^r$  are random variables distributing uniformly in  $[0, 2\pi)$  [72]. Notice that  $|r\rangle$  is not normalized because  $\langle r|r\rangle = N_{\text{st}}$ .

We now define a statistical average as

$$\langle\langle \cdots \rangle\rangle = \lim_{R \rightarrow \infty} \frac{1}{R} \sum_{r=1}^R \cdots, \quad (10)$$

where  $r$  denotes a different set of the random variables. Since  $\langle\langle e^{i\theta_x^r} \rangle\rangle = 0$  and  $\langle\langle (e^{i\theta_{x'}^r})^* e^{i\theta_x^r} \rangle\rangle = \langle\langle e^{i(\theta_x^r - \theta_{x'}^r)} \rangle\rangle = \delta_{xx'}$ , we can

easily show that  $|r\rangle$ 's are statistically complete

$$\langle\langle |r\rangle\langle r| \rangle\rangle = \sum_{x=1}^{N_{\text{st}}} |x\rangle\langle x| = \hat{1}. \quad (11)$$

The expectation value of operator  $\hat{O}$  with respect to  $|r\rangle$  is given by

$$\langle r|\hat{O}|r\rangle = \sum_{x=1}^{N_{\text{st}}} \langle x|\hat{O}|x\rangle + \sum_{x=1}^{N_{\text{st}}} \sum_{x'=1}^{N_{\text{st}}} (e^{i(\theta_x^r - \theta_{x'}^r)} - \delta_{xx'}) \langle x'|\hat{O}|x\rangle. \quad (12)$$

Therefore, the trace can be evaluated stochastically as

$$\text{Tr}[\hat{O}] = \sum_{x=1}^{N_{\text{st}}} \langle x|\hat{O}|x\rangle = \langle\langle r|\hat{O}|r\rangle\rangle. \quad (13)$$

Finally, if the statistical average is truncated at a finite number  $R$  of the random-phase states in Eq. (13), the leading error  $|\delta O|$ , where  $\delta O$  is the second term of the right-hand side of Eq. (12), is estimated as [70, 71]

$$\begin{aligned} |\delta O|^2 &= \frac{1}{R} \sum_{x \neq x'} |\langle x'|\hat{O}|x\rangle|^2 \\ &= \frac{1}{R} \left( \text{Tr}[\hat{O}^2] - \sum_{x=1}^{N_{\text{st}}} \langle x|\hat{O}|x\rangle^2 \right). \end{aligned} \quad (14)$$

Here,  $\hat{O}$  is assumed to be a Hermitian operator. Note, however, that  $\hat{O} = e^{-\beta\hat{H}}\hat{A}$  is not Hermitian if  $\hat{A}$  does not commute with  $\hat{H}$ , even if  $\hat{A}$  itself is Hermitian. In such a case,  $\hat{O}$  can still be chosen Hermitian if the symmetric form

$$\hat{O} = e^{-\beta\hat{H}/2}\hat{A}e^{-\beta\hat{H}/2} \quad (15)$$

is used as in Eq. (5).

### C. Finite-temperature Lanczos method

From Eqs. (10) and (13) we obtain

$$Z = \lim_{R \rightarrow \infty} \frac{1}{R} \sum_{r=1}^R \langle r|e^{-\beta\hat{H}}|r\rangle. \quad (16)$$

Now the matrix element  $\langle r|e^{-\beta\hat{H}}|r\rangle$  has to be evaluated. If the full diagonalization of  $\hat{H}$  were possible, the matrix element could be evaluated exactly by inserting the identity with the eigenstates  $\hat{P}_{\text{Eig}} = \sum_{n=1}^{N_{\text{st}}} |E_n\rangle\langle E_n| = \hat{1}$ . In the finite-temperature Lanczos method,  $\hat{P}_{\text{Eig}}$  is approximated by the projection onto the Ritz states  $\hat{P}_{\text{Ritz}} = \sum_{l=1}^{N_L} |\epsilon_l^r\rangle\langle \epsilon_l^r|$ , where  $|\epsilon_l^r\rangle$  is the  $l$ -th Ritz state associated with the Ritz value  $\epsilon_l^r$  obtained by the Lanczos algorithm terminated at the  $N_L$ th step of the Lanczos iteration started with the initial state  $|r\rangle$ . The partition function is thus approximated as

$$Z \approx \frac{1}{R} \sum_{r=1}^R \langle r|e^{-\beta\hat{H}}|r\rangle \approx \frac{1}{R} \sum_{r=1}^R \sum_{l=1}^{N_L} e^{-\beta\epsilon_l^r} |\langle \epsilon_l^r|r\rangle|^2, \quad (17)$$

where the first approximation is made by truncating the number of the random states at a finite value  $R$ , and the second approximation is made by approximating the Boltzmann factor as  $e^{-\beta\hat{H}} \approx e^{-\beta\hat{H}} \hat{P}_{\text{Ritz}} = \sum_{l=1}^{N_L} e^{-\beta\epsilon_l^r} |\epsilon_l^r\rangle\langle\epsilon_l^r|$ . Equation (17) is the approximate partition function calculated in the finite-temperature Lanczos method [67–69]. Notice that since  $|r\rangle$  defined in Eq. (9) is not normalized, differently from Refs. [67–69], the factor  $N_{\text{st}}$  does not appear in Eq. (17). Such a factor is taken into account in  $|\langle\epsilon_l^r|r\rangle|^2$  in our formulation.

#### D. Block Lanczos algorithm

Here, we describe the block Lanczos algorithm [73–76] to adopt it for the finite-temperature Lanczos method. As the initial states, we first generate  $M_B$  random-phase states

$$|r_1\rangle, |r_2\rangle, \dots, |r_{M_B}\rangle. \quad (18)$$

To describe the algorithm, it is convenient to move to the matrix notation. Let  $\mathbf{Y} \in \mathbb{C}^{N_{\text{st}} \times M_B}$  be a matrix representation of the set of random-phase states in Eq. (18) in the orthonormal basis  $\{|x\rangle\}$  used in Eq. (9), i.e.,

$$[\mathbf{Y}]_{xb} = \langle x|r_b\rangle = e^{i\theta_{xb}^r}. \quad (19)$$

Namely,  $\mathbf{Y}$  contains  $M_B$  random-phase vectors as column vectors.

Since the  $M_B$  random-phase vectors are not orthonormalized each other,  $\mathbf{Y}$  itself cannot be used as the initial vectors for the block Lanczos algorithm. Instead,  $M_B$  orthonormalized vectors can be obtained from a QR factorization of  $\mathbf{Y}$  as

$$\mathbf{Y} = \mathbf{Q}_1 \mathbf{B}_0, \quad (20)$$

where  $\mathbf{Q}_1 \in \mathbb{C}^{N_{\text{st}} \times M_B}$  satisfies  $\mathbf{Q}_1^\dagger \mathbf{Q}_1 = \mathbf{I}$  and  $\mathbf{B}_0 \in \mathbb{C}^{M_B \times M_B}$  is an upper triangular matrix satisfying  $\mathbf{Y}^\dagger \mathbf{Y} = \mathbf{B}_0^\dagger \mathbf{B}_0$ . Now  $\mathbf{Q}_1$  can be used as the initial vectors for the block-Lanczos algorithm. Block-Lanczos vectors  $\mathbf{Q}_2, \mathbf{Q}_3, \dots, \mathbf{Q}_{k_{\text{max}}}$  with  $k_{\text{max}} = N_L/M_B$  are constructed successively by iterating the following procedures for  $k = 1$  to  $k_{\text{max}}$ :

$$\mathbf{A}_k := \mathbf{Q}_k^\dagger \mathbf{H} \mathbf{Q}_k \quad (21)$$

$$\mathbf{X}_k := \mathbf{H} \mathbf{Q}_k - \mathbf{Q}_k \mathbf{A}_k - \mathbf{Q}_{k-1} \mathbf{B}_{k-1}^\dagger \quad (22)$$

$$\mathbf{X}_k = \mathbf{Q}_{k+1} \mathbf{B}_k, \quad (23)$$

where  $\mathbf{Q}_0 := \mathbf{0}$  and  $[\mathbf{H}]_{xx'} = \langle x|\hat{H}|x'\rangle$  is the matrix representation of  $\hat{H}$ . The procedure in Eq. (23) should be read as the QR factorization of  $\mathbf{X}_k \in \mathbb{C}^{N_{\text{st}} \times M_B}$  yielding the  $(k+1)$ st block-Lanczos vectors  $\mathbf{Q}_{k+1} \in \mathbb{C}^{N_{\text{st}} \times M_B}$  and an upper-triangular matrix  $\mathbf{B}_k \in \mathbb{C}^{M_B \times M_B}$ . The procedure in Eq. (21) requires  $M_B$  matrix-vector multiplications. Note that  $N_L$  is assumed to be a multiple of  $M_B$  for simplicity. However, if  $N_L$  is not a multiple of  $M_B$ ,  $k_{\text{max}}$  should be read as  $\text{nint}(N_L/M_B)$  for example and  $N_L$  below as  $k_{\text{max}} M_B$ , where  $\text{nint}(\cdot)$  denotes the nearest-integer function.

Defining  $\tilde{\mathbf{Q}}_k = (\mathbf{Q}_1, \dots, \mathbf{Q}_k) \in \mathbb{C}^{N_{\text{st}} \times k M_B}$ ,  $\mathbf{T}_k = \tilde{\mathbf{Q}}_k^\dagger \mathbf{H} \tilde{\mathbf{Q}}_k \in \mathbb{C}^{k M_B \times k M_B}$  can be constructed after the procedure (21) of the

$k$ th block-Lanczos iteration. It follows from Eqs. (21)–(23) that  $\mathbf{Q}_j^\dagger \mathbf{H} \mathbf{Q}_j = \mathbf{A}_j \delta_{j,j} + \mathbf{B}_j \delta_{j,j+1} + \mathbf{B}_j^\dagger \delta_{j,j-1}$ . Therefore,  $\mathbf{T}_k$  is a Hermitian-band matrix of the form

$$\mathbf{T}_k = \begin{bmatrix} \mathbf{A}_1 & \mathbf{B}_1^\dagger & 0 & \cdots & 0 \\ \mathbf{B}_1 & \mathbf{A}_2 & \mathbf{B}_2^\dagger & \ddots & \vdots \\ 0 & \ddots & \ddots & \ddots & 0 \\ \vdots & \ddots & \mathbf{B}_{k-2} & \mathbf{A}_{k-1} & \mathbf{B}_{k-1}^\dagger \\ 0 & \cdots & 0 & \mathbf{B}_{k-1} & \mathbf{A}_k \end{bmatrix}. \quad (24)$$

A diagonalization of  $\mathbf{T}_{k_{\text{max}}}$  gives  $N_L$  Ritz values as its eigenvalues, i.e.,

$$\mathbf{D} = \mathbf{U}^\dagger \mathbf{T}_{k_{\text{max}}} \mathbf{U} = \text{diag}(\epsilon_1^{(r)}, \dots, \epsilon_{N_L}^{(r)}), \quad (25)$$

where  $\mathbf{U}$  is a unitary matrix. Here, the superscript  $\{r\}$  denotes that the Ritz values are obtained by the block-Lanczos method with the initial states  $\{r\} = \{r_1, r_2, \dots, r_{M_B}\}$ . It follows from Eq. (25) and  $\mathbf{T}_{k_{\text{max}}} = \tilde{\mathbf{Q}}_{k_{\text{max}}}^\dagger \mathbf{H} \tilde{\mathbf{Q}}_{k_{\text{max}}}$  that  $\mathbf{D} = (\tilde{\mathbf{Q}}_{k_{\text{max}}} \mathbf{U})^\dagger \mathbf{H} (\tilde{\mathbf{Q}}_{k_{\text{max}}} \mathbf{U})$ . Therefore, the Ritz state  $|\epsilon_l^{(r)}\rangle$  which satisfies  $\hat{H}|\epsilon_l^{(r)}\rangle = \epsilon_l^{(r)}|\epsilon_l^{(r)}\rangle$  and  $\langle\epsilon_l^{(r)}|\epsilon_l^{(r)}\rangle = \delta_{ll'}$  is given by

$$\langle x|\epsilon_l^{(r)}\rangle = [\tilde{\mathbf{Q}}_{k_{\text{max}}} \mathbf{U}]_{xl}. \quad (26)$$

Finally, the overlap between the initial state and the  $l$ -th Ritz state is given by

$$\begin{aligned} \langle\epsilon_l^{(r)}|r_b\rangle &= \left[ \mathbf{U}^\dagger \tilde{\mathbf{Q}}_{k_{\text{max}}}^\dagger \mathbf{Y} \right]_{lb} = \left[ \mathbf{U}^\dagger \tilde{\mathbf{Q}}_{k_{\text{max}}}^\dagger \mathbf{Q}_1 \mathbf{B}_0 \right]_{lb} \\ &= \sum_{m=1}^{M_B} [\mathbf{U}^\dagger]_{lm} [\mathbf{B}_0]_{mb}, \end{aligned} \quad (27)$$

where  $\mathbf{Q}_j^\dagger \mathbf{Q}_j = \delta_{j,j} \mathbf{I}$  is used in the last equality.

#### E. Block-extended finite-temperature Lanczos method

Now the block-extended version of the finite-temperature Lanczos method can be formulated. For simplicity, we assume that the number  $R$  of the random-phase states is multiple of the number  $M_B$  of the block size. Introducing

$$R_B = \frac{R}{M_B}, \quad (28)$$

the approximate partition function in Eq. (17) can be expressed as

$$\begin{aligned} Z &\approx \frac{1}{R} \sum_{r=1}^R \langle r|e^{-\beta\hat{H}}|r\rangle = \frac{1}{R_B M_B} \sum_{r=1}^{R_B} \sum_{b=1}^{M_B} \langle r_b|e^{-\beta\hat{H}}|r_b\rangle \\ &\approx \frac{1}{R_B} \sum_{r=1}^{R_B} \sum_{l=1}^{N_L} e^{-\beta\epsilon_l^{(r)}} \left( \frac{1}{M_B} \sum_{b=1}^{M_B} |\langle\epsilon_l^{(r)}|r_b\rangle|^2 \right). \end{aligned} \quad (29)$$

On the equality of the first line, the  $R (= R_B M_B)$  random-phase states are simply re-labeled by a combination of the

subscripts  $r$  and  $b$ . To obtain the second line, the projection operator  $\hat{P}_{\text{Ritz}} = \sum_{l=1}^{N_L} |\epsilon_l^{(r)}\rangle\langle\epsilon_l^{(r)}|$  is inserted. A formal difference from the standard finite-temperature Lanczos method is that the overlap squared,  $|\langle\epsilon_l^{(r)}|r\rangle|^2$ , in Eq. (17) is replaced by the averaged one over the  $M_B$  random-phase states,  $\sum_{b=1}^{M_B} |\langle\epsilon_l^{(r)}|r_b\rangle|^2/M_B$ , in Eq. (29). Here, the overlap  $\langle\epsilon_l^{(r)}|r_b\rangle$  can be calculated through Eq. (27). Obviously, Eq. (29) reproduces Eq. (17) when  $M_B = 1$ .

Similarly to the partition function, the numerator of Eq. (5) is approximated as

$$\begin{aligned} \text{Tr} \left[ e^{-\beta\hat{H}/2} \hat{A} e^{-\beta\hat{H}/2} \right] &\approx \frac{1}{R} \sum_{r=1}^R \langle r | e^{-\beta\hat{H}/2} \hat{A} e^{-\beta\hat{H}/2} | r \rangle \\ &\approx \frac{1}{R_B} \sum_{r=1}^{R_B} \sum_{l=1}^{N_L} \sum_{l'=1}^{N_L} e^{-\beta(\epsilon_l^{(r)} + \epsilon_{l'}^{(r)})/2} \\ &\times \left( \frac{1}{M_B} \sum_{b=1}^{M_B} \langle r_b | \epsilon_{l'}^{(r)} \rangle \langle \epsilon_l^{(r)} | \hat{A} | \epsilon_{l'}^{(r)} \rangle \langle \epsilon_l^{(r)} | r_b \rangle \right). \end{aligned} \quad (30)$$

Here, the right-most expression of Eq. (5) is adopted as in the low-temperature Lanczos method [77]. If  $\hat{A}$  commutes with  $\hat{H}$ , then  $|\epsilon_l^{(r)}\rangle$  are simultaneous eigenstates of  $\hat{A}$  and  $\hat{H}$ . In this case, Eq. (30) can be further simplified because  $\langle \epsilon_{l'}^{(r)} | \hat{A} | \epsilon_l^{(r)} \rangle = A_l^{(r)} \delta_{ll'}$ , where  $A_l^{(r)}$  is an eigenvalue of  $\hat{A}$ .

A nice property of the block-extended version of the finite-temperature Lanczos method [Eqs. (29) and (30)] is that one can flexibly choose  $R_B$  and  $M_B$  to exploit the computational resource efficiently. For example, the summation  $\sum_{r=1}^{R_B} \dots$  can be done independently for each  $r$ , while a block size of  $M_B > 1$  allows for the better performance in a single process as compared to the case of  $M_B = 1$ . To be more specific, let us consider an on-the-fly Hamiltonian multiplication to the block-Lanczos vectors. In that case, the dominant computational costs are generating Hamiltonian matrix elements rather than performing simple multiply-add operations. Since the block Lanczos method multiplies the Hamiltonian matrix to  $M_B$  vectors simultaneously,  $M_B$  times less operations for generating the matrix elements are required to achieve the same number of Hamiltonian-vector multiplications, as compared to the standard Lanczos method. We remark that such simultaneous Hamiltonian multiplication to vectors can be employed also in the polynomial expansion technique [71].

In the block Lanczos method, at least  $2M_B$  vectors (of  $N_{\text{st}}$  dimension) have to be stored. When the required memory for storing the  $2M_B$  vectors exceeds the limit of the available resource, one can simply reduce the number  $M_B$  of the block size, or even switch to the standard finite-temperature Lanczos method merely by setting  $M_B = 1$ . Fortunately, the smaller number  $R$  of samplings is required for the larger  $N_{\text{st}}$  to maintain a statistical accuracy (see for example Ref. [78] and Sec. II F).

Now we have three parameters  $R_B$ ,  $M_B$ , and  $N_L$  for controlling the accuracy of the block-extended version of the finite-temperature Lanczos method. Values of these parameters will be specified for each result in Sec. III.

## F. Connection with the canonical thermal-pure-quantum state

The finite-temperature Lanczos method for observables commuting with  $\hat{H}$  [67–69], the low-temperature Lanczos method for observables not commuting with  $\hat{H}$  [77], and the block-extended version of the finite-temperature Lanczos method for observables not commuting with  $\hat{H}$  described in the previous section, can all be regarded as a method that makes use of the canonical thermal-pure-quantum (CTPQ) state [79], as recently demonstrated with the standard finite-temperature Lanczos method in Ref. [80]. For example, the matrix element  $\langle r_b | e^{-\beta\hat{H}} | r_b \rangle$  appearing in Eq. (29) is the inner product of the (unnormalized) CTPQ state  $e^{-\beta\hat{H}/2} | r_b \rangle$ . There are several ways to evaluate matrix functions operated to vectors without full diagonalization, such as polynomial expansion techniques [81–89]. With the Lanczos method used here, the CTPQ state is approximated by a linear combination of the  $N_L$  Ritz states  $|\epsilon_l^{(r)}\rangle$  as

$$e^{-\beta\hat{H}/2} | r_b \rangle \approx \hat{P}_{\text{Ritz}} e^{-\beta\hat{H}/2} | r_b \rangle = \sum_{l=1}^{N_L} e^{-\beta\epsilon_l^{(r)}/2} \langle \epsilon_l^{(r)} | r_b \rangle |\epsilon_l^{(r)}\rangle. \quad (31)$$

In this sense, although it is difficult to estimate the systematic error associated with the approximation made in Eq. (31), one can still refer to the convergence analysis of CTPQ states [79]. For instance, the better convergence in probability to the ensemble average is expected for the larger  $\mathcal{D}(T) = e^{Ls(T)}$  with  $s(T)$  being the entropy density. Here  $\mathcal{D}(T)$  can be interpreted as a temperature-dependent effective dimension of the Hilbert space, because it satisfies  $\lim_{T \rightarrow \infty} \mathcal{D}(T) = N_{\text{st}}$  and  $\lim_{T \rightarrow 0} \mathcal{D}(T) = g$ , where  $g$  is the ground-state degeneracy.

Note that the (block) Lanczos method approximates well the extremal eigenvalues and eigenstates within a few hundreds of the Lanczos steps  $N_L$ , almost independently of the realization of the initial random-phase state  $|r_b\rangle$ . Therefore, the (block) Lanczos approach to the matrix exponential, as in Eq. (31), complements the CTPQ approach at low temperatures by its fast convergence to the ground state and low-lying excited states for each symmetry sector. In particular, the block Lanczos method can better approximate the low-lying excited states, especially within the block size, as compared to the standard Lanczos method [73]. On the other hand, empirically, the convergence of the (block) Lanczos method to the inner (i.e., non extremal) eigenpairs with dense spectra seems “random”, in the sense that the convergence depends on the realization of  $|r_b\rangle$  for fixed  $N_L$ , as observed in spectra of dynamical correlation functions [69]. This implies that relatively large error bars are expected at temperatures where the specific heat exhibits a peak, because the larger specific heat indicates the larger fluctuation of the internal energy  $\langle \hat{H} \rangle$ , thus implying the denser eigen spectra of  $\hat{H}$ . Finally, we remark that a connection between the finite-temperature Lanczos method and the eigenstate-thermalization hypothesis [90, 91] has been discussed recently in Ref. [92].



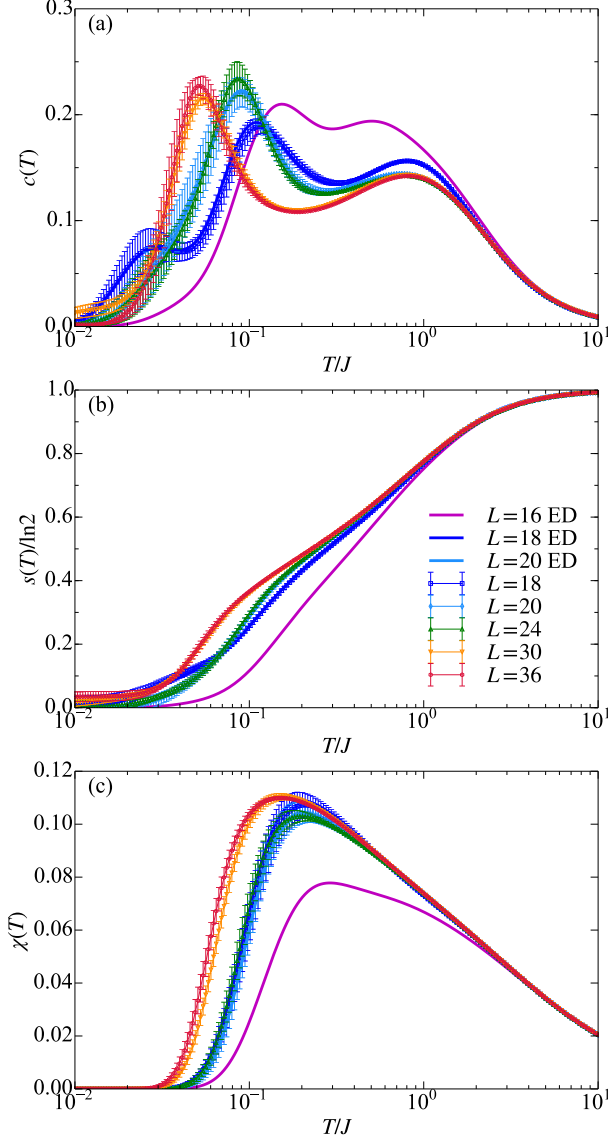


FIG. 3. (a) Specific heat  $c(T)$ , (b) entropy density  $s(T)$ , and (c) uniform susceptibility  $\chi(T)$  at  $J_c/J = 0.07$  for  $L = 4 \times 4$ ,  $18$ ,  $5 \times 4$ ,  $6 \times 4$ ,  $30$ , and  $6 \times 6$  clusters (see Fig. 4). Solid lines are results obtained by the full exact diagonalization. Block-Lanczos parameters are  $R_B = 24$ ,  $M_B = 6$ , and  $N_L = 120$  for  $L = 4 \times 5$ ,  $R_B = 24$ ,  $M_B = 8$ , and  $N_L = 160$  for  $L = 18$ ,  $R_B = 8$ ,  $M_B = 8$ , and  $N_L = 200$  for  $L = 6 \times 4$ ,  $R_B = 6$ ,  $M_B = 8$ , and  $N_L = 320$  for  $L = 30$ , and  $R_B = 6$ ,  $M_B = 4$  for  $0 \leq |S_z| \leq 1$ ,  $M_B = 6$  for  $2 \leq |S_z| \leq 5$ ,  $M_B = 6$  for  $6 \leq |S_z|$ , and  $N_L = 720$  for  $L = 6 \times 6$ .

### III. RESULTS

Figure 3 shows the specific heat

$$c(T) = \frac{1}{LT^2} \left[ \langle \hat{H}^2 \rangle - \langle \hat{H} \rangle^2 \right], \quad (32)$$

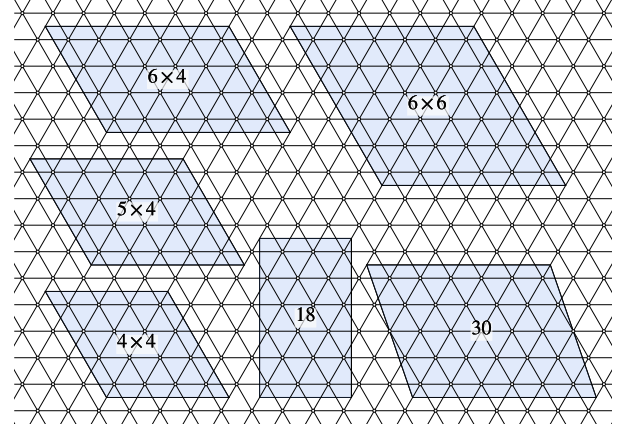


FIG. 4. Cluster structures used for the calculations.

the entropy density

$$s(T) = \frac{1}{LT} \left[ \langle \hat{H} \rangle + T \ln Z \right], \quad (33)$$

and the uniform magnetic susceptibility

$$\chi(T) = \frac{1}{LT} \left[ \langle (\hat{S}^z)^2 \rangle - \langle \hat{S}^z \rangle^2 \right] \quad (34)$$

at  $K/J = 0.07$  for  $L = 4 \times 4$ ,  $18$ ,  $5 \times 4$ ,  $6 \times 4$ ,  $30$ , and  $6 \times 6$  (see Fig. 4). Notice that the entropy density  $s(T)$  is normalized with respect to  $\lim_{T \rightarrow \infty} s(T) = \ln 2$  in the figure. Since these three quantities involve only the thermal average of the quantities that commute with  $\hat{H}$ , the calculations are particularly efficient as compared to the quantities that do not commute with  $\hat{H}$ . Statistical errors are estimated from the unbiased estimation of standard deviation

$$\tilde{\sigma} = \sqrt{\frac{1}{R_B - 1} \sum_{r=1}^{R_B} (X_r - \bar{X})^2}, \quad (35)$$

where  $X_r$  is calculated  $c(T)$ ,  $s(T)$ , or  $\chi(T)$  but for a given  $r$  (without averaging over  $r$ ), and  $\bar{X}$  is  $c(T)$ ,  $s(T)$ , or  $\chi(T)$  itself. For comparison, the full-diagonalization results are also shown in Fig. 3 for  $L \leq 20$ . It is confirmed for  $L = 18$  and  $L = 5 \times 4$  that the results obtained by the block-extended version of the finite-temperature Lanczos method coincide with the full-diagonalization results within error bars.

Figure 5 shows the  $J_c$  dependence of  $c(T)$ ,  $s(T)$ ,  $\chi(T)$ , and a generalized temperature-dependent Wilson ratio

$$R_W(T) = \frac{4\pi^2 T \chi(T)}{3s(T)} \quad (36)$$

recently introduced in Ref. [93] for  $L = 36$ , which is the largest cluster available and preserves all the symmetries of the triangular lattice. The error bars for  $R_W(T)$  are obtained in the same way for  $c(T)$ ,  $s(T)$ , and  $\chi(T)$ . Without the ring-exchange interaction ( $J_c/J = 0$ ),  $c(T)$  exhibits a peak

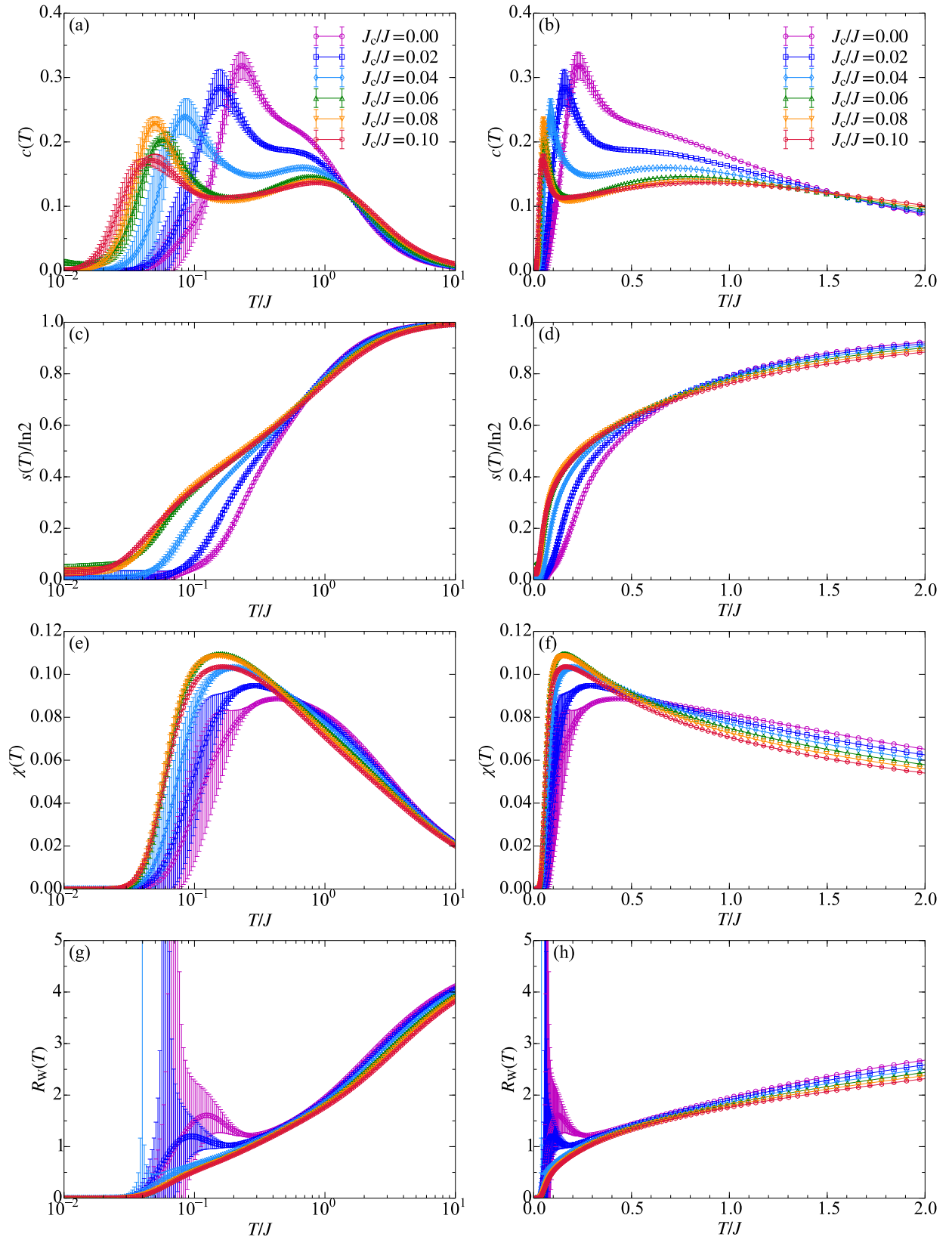


FIG. 5. Semi-log (left) and linear (right) plots of (a,b) specific heat  $c(T)$ , (c,d) entropy density  $s(T)$ , (e,f) uniform susceptibility  $\chi(T)$ , and (g,h) Wilson ratio  $R_W(T)$  for several  $J_c/J$  values indicated in the figures. The  $L = 6 \times 6$  cluster is used for the calculations. Block-Lanczos parameters are  $R_B = 6$ ,  $M_B = 4$  for  $0 \leq |S_z| \leq 1$ ,  $M_B = 6$  for  $2 \leq |S_z| \leq 5$ ,  $M_B = 6$  for  $6 \leq |S_z|$ , and  $N_L = 720$ .

around  $T/J = 0.2$  and a broad shoulder for  $T/J \gtrsim 0.5$ , while no significant structure can be found in  $s(T)$ . This is in good agreement with the previous results calculated by the finite-temperature Lanczos and the exponential tensor-renormalization-group methods [66, 94–96].

For  $J_c/J \geq 0.04$ , the specific heat  $c(T)$  shows a double-peak structure with a broad high-temperature peak around  $T_{\text{high}}/J \sim 1$  and a sharp low-temperature peak  $T_{\text{low}}/J \ll 1$ . As shown in Fig. 3(a), the low-temperature peak position for  $J_c/J = 0.07$  tends to be lowered for the larger clusters, while the high-temperature peak is insensitive to the system size. For example, for the  $L = 6 \times 6$  cluster, the high-temperature peak appears at  $T_{\text{high}}/J \approx 0.8$  and the low-temperature peak is found at  $T_{\text{low}}/J \approx 0.05$ . At the highest temperature around  $T/J \sim 10$ , the entropy density reaches  $s = \ln 2 \approx 0.693$ , indicating that the system is in the paramagnetic state. In the temperature regime where  $c(T)$  shows a dip between the two peaks,  $s(T)$  exhibits a shoulder-like structure which is visible in the semi-log plot shown in Fig. 5(c). Interestingly, about the half of the total entropy  $s = \frac{1}{2} \ln 2 \approx 0.347$  remains at such a temperature regime. The shoulder-like structure of  $s(T)$  becomes more prominent for the larger system size [see Fig. 3(b)].

As shown in Figs. 5(e) and 5(f), the uniform magnetic susceptibility  $\chi(T)$  decreases quickly below temperature  $T_\chi$  at which  $\chi(T)$  takes a maximum. The peak position  $T_\chi$  varies from  $T_\chi \approx 0.3J$  for  $J_c/J = 0$  to  $T_\chi \approx 0.15J$  for  $J_c/J = 0.1$ . In particular, a rapid decrease of  $T_\chi$  can be observed for  $0 \leq J_c/J \leq 0.06$ . It is also found that for  $J_c/J \geq 0.02$  there exists a temperature region where the entropy and specific heat are finite while  $\chi(T)$  is almost zero. This implies that many non-magnetic excitations exist below the first magnetic excitation.

Such characteristic low-lying excitations can be better seen in the temperature-dependent Wilson ratio  $R_W(T)$  [93] shown in Figs. 5(g) and 5(h). If this quantity tends to zero, it is indicative that the magnetic excitations are inactive while non-magnetic ones are active. Although error bars are too large to discuss its behavior for  $T/J < 0.1$  and  $J_c/J \leq 0.02$ , the slight upturn of  $R(T)$  for  $T/J \sim 0.2$  and  $J_c/J = 0$  is consistent with the result for the pure-triangular case reported in Ref. [93]. Despite the large error bars, one can still see a clear change of behavior in  $R_W(T)$  for  $T/J < 0.4$  between the parameter regions  $J_c/J \leq 0.02$  and  $J_c/J \geq 0.04$ .

Finally, it is observed in Fig. 5 that the error bars become larger below the temperature at which the specific heat takes the maximum (the low-temperature maximum for  $J \geq 0.04$ ). This behavior is expected from the discussion in Sec. II F.

#### IV. SUMMARY AND DISCUSSION

The thermodynamic properties of an  $S = 1/2$  antiferromagnetic Heisenberg model on the triangular lattice with the ring-exchange interaction have been studied by the block-extended version of the finite-temperature Lanczos method. The results for entropy  $s(T)$ , uniform magnetic susceptibility  $\chi(T)$ , and Wilson ratio  $R_W(T)$  have shown that there exist low-

energy non-magnetic excitations for  $J_c/J \geq 0.04$ . At the same time, the specific heat  $c(T)$  shows a characteristic double-peak structure for  $J_c/J \geq 0.04$ .

As it is apparent from  $s(T)$ ,  $\chi(T)$ , and  $R_W(T)$ , there is a great deal of similarity in the low-lying excitations between the ring-exchange model studied here and the  $J_1 - J_2$  model on the triangular lattice or the kagome-lattice antiferromagnet [66, 93, 97, 98]. However, the double-peak structure found here in  $c(T)$  for  $J_c/J \geq 0.04$  distinguishes the ring-exchange model from the other models. Indeed, such a double-peak structure has not been observed in the  $J_1 - J_2$  model on the triangular lattice for  $J_2/J_1 = 0.1$  and  $0.2$  [94]. Moreover, the separation of the two peaks is found to be more pronounced with increasing the system size. Such a system-size dependence of the low-temperature peak positions is in contrast to that in the kagome-lattice antiferromagnet where the lower-temperature peak moves towards higher temperatures with increasing the system size [78, 99]. Instead, a system-size dependence similar to the ring-exchange model found here has also been observed in the Kitaev model [100]. This implies that the excitations corresponding to the high-temperature peak are spatially local, while those corresponding to the low-temperature peak are not.

It is interesting to compare the present results with the recent experiments on  $\text{Ba}_2\text{CoNb}_6\text{O}_{24}$ , which is considered to be the  $S = 1/2$  two-dimensional triangular-lattice Heisenberg antiferromagnet, with a nearest-neighbor coupling  $J = 0.144$  meV [64] or  $J = 1.66 \pm 0.06$  K [65]. In this material, no indication of the magnetic order has been found in the thermodynamic measurements down to  $T = 80$  mK. After subtraction of the phonon contribution ( $\propto T^3$ ), the specific heat takes a single-peak structure. Considering the absence of the double-peak structure in the specific heat, the case without the ring-exchange interaction (i.e.,  $J_c/J = 0$ ) is rather more relevant to  $\text{Ba}_2\text{CoNb}_6\text{O}_{24}$  than the ring-exchange model. In the literature [64, 65], the absence of the  $120^\circ$  long-range order at finite temperatures is attributed to a realization of the Mermin-Wagner theorem [101] on the real material.

In Appendix B, we study the effect of ring-exchange interaction  $J_c$  on the spin-wave dispersion in the  $120^\circ$  ordered state, within the linear spin-wave theory. It is found that the spin-excitation energies near the  $M$  point and symmetrically equivalent points are decreased drastically with  $J_c$ . However, the spin-wave analysis, which takes into account only the magnon excitation, was not able to capture the characteristic thermodynamic features, including the double-peak structure of  $c(T)$ , found in our numerical calculations. In particular, the microscopic understanding of the double-peak structure in  $c(T)$  found here deserves a rather systematic analysis for larger clusters and is left for the future study.

#### ACKNOWLEDGMENTS

The authors are grateful to Tao Li for useful discussions and Yusuke Nomura and Shohei Miyakoshi for helpful comments. The numerical computations have been done on HOKUSAI GreatWave and HOKUSAI BigWaterfall super-



computers at RIKEN under Project No. G19011. This work was supported by Grant-in-Aid for Research Activity start-up (No. 19K23433) and Grant-in-Aid for Scientific Research (B) (No. 18H01183) from MEXT, Japan.

#### Appendix A: Algorithm to find a spin configuration for a given state label in a fixed-magnetization Hilbert space

The two-dimensional search technique introduced by Lin [102] is an efficient method to find a state label  $j$  for a given spin configuration  $i$ , i.e.,  $j(i)$ , with relatively small amount of storage, whose dimension is  $2 \times 2^{L/2}$ . Here, a set of the binary digits  $\{b_l\}$  that represents  $i$  with

$$i = \sum_{l=1}^L b_l 2^{l-1} \equiv (b_L b_{L-1} \dots b_1)_2 \quad (\text{A1})$$

is assigned to a spin configuration, by identifying  $b_l = 0$  ( $b_l = 1$ ) with the presence of a spin- $\downarrow$  (spin- $\uparrow$ ) at the  $l$ th site.

The inverse table, which returns a spin configuration  $i$  for a given state label  $j$ , i.e.,  $i(j)$ , is often stored. For a fixed-magnetization Hilbert space, the length of the inverse table is given by the binomial coefficient

$$\binom{L}{N_\uparrow} = \frac{L!}{N_\uparrow! (L - N_\uparrow)!} = \binom{L}{L - N_\uparrow}, \quad (\text{A2})$$

where  $N_\sigma$  is the number of spins with spin  $\sigma$ ,  $N_\uparrow + N_\downarrow = L$ , and the magnetization is given by  $S^z = (N_\uparrow - N_\downarrow)/2$ . The range of the state label  $j$  can be chosen as

$$1 \leq j \leq \binom{L}{N_\uparrow}. \quad (\text{A3})$$

For a concrete example of the correspondence between  $j$  and  $i$ , see Table I. Since the range of  $i$  is given by

$$2^{N_\uparrow} - 1 \leq i \leq 2^L - 2^{L-N_\uparrow}, \quad (\text{A4})$$

$i$  might be 64 bit integer for  $L \geq 32$ . An algorithm that returns a spin configuration  $i$  for a given state label  $j$  may be useful when spin configurations  $i$  do not appear sequentially during the calculation of matrix elements of the Hamiltonian, due to, for example, a parallelization of the on-the-fly matrix-vector multiplication.

Here we introduce such a function  $i(j)$  by assuming that both  $i$  and  $j$  are in the ascending order, as in Table I. The basic idea is to assign a state label  $j$  to one of the shortest paths from the vertex  $\binom{L}{L-N_\uparrow}$  to the topmost vertex  $\binom{0}{0}$  on the Pascal's triangle (see Fig. 6). Since there are  $\binom{L}{L-N_\uparrow}$  different paths, a one-to-one correspondence between the shortest paths and  $\{j\}$  should exist.

To find a correspondence between binary numbers and the shortest paths on the Pascal's triangle, the following combinatorial recursion formula should be reminded;

$$\binom{L}{L-N_\uparrow} = \binom{L-1}{L-N_\uparrow-1} + \binom{L-1}{L-N_\uparrow}. \quad (\text{A5})$$

TABLE I. Correspondence between state label  $j$  and spin configuration  $i$  for  $L = 6$  and  $N_\uparrow = 3$ . Both  $j$  and  $i$  are assumed to be in the ascending order.

$j$	$i(L, N_\uparrow, j)$	$j$	$i(L, N_\uparrow, j)$
1	(000111) <sub>2</sub> = 7	11	(100011) <sub>2</sub> = 35
2	(001011) <sub>2</sub> = 11	12	(100101) <sub>2</sub> = 37
3	(001101) <sub>2</sub> = 13	13	(100110) <sub>2</sub> = 38
4	(001110) <sub>2</sub> = 14	14	(101001) <sub>2</sub> = 41
5	(010011) <sub>2</sub> = 19	15	(101010) <sub>2</sub> = 42
6	(010101) <sub>2</sub> = 21	16	(101100) <sub>2</sub> = 44
7	(010110) <sub>2</sub> = 22	17	(110001) <sub>2</sub> = 49
8	(011001) <sub>2</sub> = 25	18	(110010) <sub>2</sub> = 50
9	(011010) <sub>2</sub> = 26	19	(110100) <sub>2</sub> = 52
10	(011100) <sub>2</sub> = 28	20	(111000) <sub>2</sub> = 56

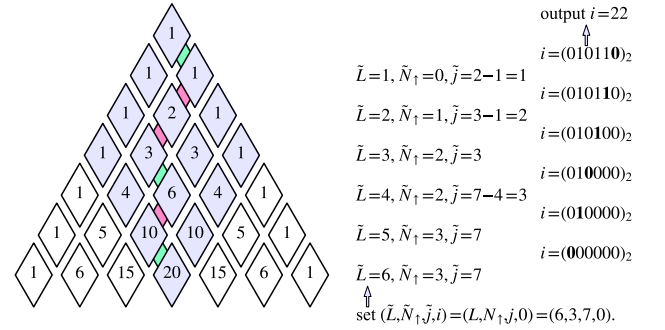


FIG. 6. Schematic figure of the algorithm to find a spin configuration  $i$  for a given state label  $j$ . The figure should be read from bottom to top to compare with Algorithm 1. For a given set of  $L$ ,  $N_\uparrow$ , and  $j$ , one of the shortest paths from the vertex  $\binom{L}{L-N_\uparrow}$  to the topmost vertex  $\binom{0}{0}$  of the Pascal's triangle is assigned, and the path determines the spin configuration  $i = \sum_{l=1}^L b_l 2^{l-1} = (b_L b_{L-1} \dots b_1)_2$ . The path goes rightward if  $\tilde{j} > \binom{L-1}{N_\uparrow}$  (indicated by magenta), or else leftward (indicated by green). The rightward (leftward) path from  $\tilde{L}$ th row to  $\tilde{L}-1$ th row implies that  $b_{\tilde{L}} = 1$  ( $b_{\tilde{L}} = 0$ ). The figure refers to the input  $(L, N_\uparrow, j) = (6, 3, 7)$ , which results in the output  $i = (010110)_2 = 22$ . The  $(N_\uparrow + 1) \times (N_\downarrow + 1) = 16$  vertices on the possible  $\binom{6}{3} = 20$  shortest paths are highlighted with shaded blue color, and  $b_{\tilde{L}}$  in  $i$  is highlighted with boldface. Although a quick return is possible at  $\tilde{L} = 3$  in this example, according to the lines 9–11 of Algorithm 1, the remaining processes corresponding to the lines 12–15 of Algorithm 1 for  $\tilde{L} \leq 3$  are also shown here in this figure.

In terms of the Pascal's triangle, Eq. (A5) relates the current vertex (left-hand side) with its upper left vertex (first term of the right-hand side) and upper right vertex (second term of the right-hand side). More specifically, among the total  $\binom{L}{L-N_\uparrow}$  spin configurations,  $\binom{L-1}{L-N_\uparrow-1} = \binom{L-1}{N_\uparrow}$  spin configurations have “0” at the  $L$ th binary digit, and  $\binom{L-1}{L-N_\uparrow} = \binom{L-1}{N_\uparrow-1}$  spin configurations have “1” at the  $L$ th binary digit, assuming that the number of 1’s is  $N_\uparrow$ . By taking into account also the assumption that both  $i$  and  $j$  are in the ascending order with Eq. (A3),

the  $L$ th binary digit  $b_L$  of  $i$  for a given  $j$  is determined as

$$b_L = \begin{cases} 0 & \text{if } j \leq \binom{L-1}{N_\uparrow}, \\ 1 & \text{otherwise.} \end{cases} \quad (\text{A6})$$

This property holds for any  $(L, N_\uparrow, j)$ , implying that  $i$  can be determined by repeatedly evaluating the above for the remaining binary digits  $\{b_l\}_{l=1}^{L-1}$  with a proper manipulation (decrement) of  $(L, N_\uparrow, j)$ . A proposed function of finding a spin configuration  $i$  for a given set of  $(L, N_\uparrow, j)$  is summarized in Algorithm 1.

**Algorithm 1** A function that returns a spin configuration  $i$  for given number of site  $L$ , number of up spins  $N_\uparrow$ , and state label  $j$ . Comments are given in the right-most side.

**Require:**

**Input:** integer  $L, N_\uparrow$ , and  $j$

$0 \leq N_\uparrow \leq L$

$1 \leq j \leq \binom{L}{N_\uparrow}$

Temporal integer variables  $\tilde{L}, \tilde{N}_\uparrow$ , and  $\tilde{j}$

**Ensure:**

**Output:** integer  $i$

$2^{N_\uparrow} - 1 \leq i \leq 2^L - 2^{L-N_\uparrow}$

```

1: function FIND-CONFIGURATION( $L, N_\uparrow, j$ )
2:    $i = 0$                                 ▶ initialization
3:    $\tilde{j} = j$                                 ▶ initialization
4:    $\tilde{N}_\uparrow = N_\uparrow$                           ▶ initialization
5:   for  $\tilde{L} = L, L-1, \dots, 1$  do          ▶ sweep all binary digits of  $i$ 
6:     if  $\tilde{j} = 1$  then
7:        $i = i + 2^{\tilde{N}_\uparrow} - 1$                   ▶ Eq. (A7)
8:       return  $i$                             ▶  $i$  is determined
9:     else if  $\tilde{j} = \binom{\tilde{L}}{\tilde{N}_\uparrow}$  then
10:       $i = i + 2^{\tilde{L}} - 2^{\tilde{L}-\tilde{N}_\uparrow}$             ▶ Eq. (A8)
11:      return  $i$                             ▶  $i$  is determined
12:     else if  $\tilde{j} > \binom{\tilde{L}-1}{\tilde{N}_\uparrow}$  then
13:       $i = i + 2^{\tilde{L}-1}$                       ▶  $\tilde{L}$ th binary digit of  $i$  is 1
14:       $\tilde{j} = \tilde{j} - \binom{\tilde{L}-1}{\tilde{N}_\uparrow}$                 ▶ to satisfy Eq. (A9)
15:       $\tilde{N}_\uparrow = \tilde{N}_\uparrow - 1$                   ▶ decrement “# of  $\uparrow$  spins” by 1
16:     end if
17:   end for
18: end function

```

Several remarks on Algorithm 1 are in order.

1. Binomial coefficients should be calculated and stored in advance for the better performance.
2. Regarding the lines 3–5 of Algorithm 1, the temporal variables  $\tilde{j}$ ,  $\tilde{N}_\uparrow$ , and  $\tilde{L}$  can be considered as temporal state label, temporal number of  $\uparrow$  spins, and temporal system size, respectively. In terms of the shortest paths on the Pascal’s triangle, the decrementing loop of  $\tilde{L}$  means that the shortest path is determined by climbing up the Pascal’s triangle from its  $L$ th row, and  $\tilde{N}_\uparrow$  is the remaining number of rightward paths.  $\tilde{N}_\uparrow$  and  $\tilde{j}$  also has to be decremented properly in the loop (lines 14–15 of Algorithm 1), as it will be described in remark 5 below.

3. Regarding the lines 6–8 of Algorithm 1, the condition  $\tilde{j} = 1$  indicates that, among the remaining  $\tilde{L}$  binary digits of  $i$ , the lowest  $\tilde{N}_\uparrow$  digits should be filled with 1’s, i.e.,

$$i = (b_L b_{L-1} \dots b_{\tilde{L}+1} \underbrace{00 \dots 0}_{\tilde{L}-\tilde{N}_\uparrow} \underbrace{11 \dots 1}_{\tilde{N}_\uparrow})_2. \quad (\text{A7})$$

In terms of the shortest paths on the Pascal’s triangle, this implies that the rest of the path goes first in the upper left direction  $\tilde{L} - \tilde{N}_\uparrow$  times and then in the upper right direction  $\tilde{N}_\uparrow$  times.

4. Regarding the lines 9–11 of Algorithm 1, the condition  $\tilde{j} = \binom{\tilde{L}}{\tilde{N}_\uparrow}$  indicates that, among the remaining  $\tilde{L}$  binary digits of  $i$ , the highest  $\tilde{N}_\uparrow$  digits should be filled with 1’s, i.e.,

$$i = (b_L b_{L-1} \dots b_{\tilde{L}+1} \underbrace{11 \dots 1}_{\tilde{N}_\uparrow} \underbrace{00 \dots 0}_{\tilde{L}-\tilde{N}_\uparrow})_2. \quad (\text{A8})$$

In terms of the shortest paths on the Pascal’s triangle, this implies that the rest of the path goes first in the upper right direction  $\tilde{N}_\uparrow$  times and then in the upper left direction  $\tilde{L} - \tilde{N}_\uparrow$  times.

5. Regarding the lines 12–15 of Algorithm 1, the condition  $\tilde{j} > \binom{\tilde{L}-1}{\tilde{N}_\uparrow}$  indicates that the  $\tilde{L}$ th binary digit of  $i$  is 1, as discussed around Eqs. (A5) and (A6). In terms of the shortest paths on the Pascal’s triangle, this implies that the rightward path is chosen to go from  $\tilde{L}$ th row to  $(\tilde{L}-1)$ th row. As in line 15,  $\tilde{N}_\uparrow$  is decreased by 1 because the remaining rightward paths has to be decreased by 1. As in line 14,  $\tilde{j}$  has to be decreased in order to satisfy

$$1 \leq \tilde{j} \leq \binom{\tilde{L}}{\tilde{N}_\uparrow} \quad (\text{A9})$$

for the next loop. This allows us to make use of the relation between the combinatorial recursion and the binary digits for  $(\tilde{L}, \tilde{N}_\uparrow, \tilde{j})$ .

6. Although it is not implemented in Algorithm 1, at some  $\tilde{L}$  one can switch to refer to a “small” table  $i(\tilde{L}, \tilde{N}_\uparrow, \tilde{j})$  stored in advance in the memory to determine the remaining  $\tilde{L}$  binary digits of  $i$ , instead of fully performing the loop over  $\tilde{L}$ . One can also implement a quick return when  $\tilde{N}_\uparrow = 1$  (when the current vertex is on the line next to the right edge) or  $\tilde{L} - \tilde{N}_\uparrow = 1$  (when the current vertex is on the line next to the left edge) is satisfied.

Figure 6 shows a concrete example of the algorithm for  $L = 6$ ,  $N_\uparrow = 3$ , and  $j = 7$ . The path from the vertex  $\binom{6}{3} = 20$  to the topmost vertex is uniquely determined, and accordingly the algorithm returns the corresponding spin configuration  $i(L = 6, N_\uparrow = 3, j = 7) = (010110)_2 = 22$ .

The algorithm is applicable also to other models such as the Hubbard model where the total electron configuration can

be given as a tensor product of up-spin and down-spin electron configurations, and the  $t$ - $J$  model where the total electron configuration can be given as a tensor product of hole and spin configurations, if the Hilbert space is constructed for a fixed magnetization and number of electrons.

## Appendix B: Linear spin-wave theory

Here we study the effect of the cyclic exchange interaction  $J_c$  on the spin-wave dispersion in the  $120^\circ$  Néel ordered state within the linear spin-wave theory. A comparison of the spin-wave dispersion of the Heisenberg model on the triangular lattice with the nearest and the next-nearest-neighbor interactions ( $J$ - $J'$  model) is also be made.

### 1. Full Hamiltonian

Before starting the linear spin-wave approximation, it is convenient to rewrite the full Hamiltonian  $\hat{H}$  in terms of the sum of inner products of spin operators. The four-spin exchange term can be written as

$$\hat{P}_{ijkl} + \hat{P}_{ijkl}^\dagger = \frac{1}{4} + \sum_{i' < j' \in \langle ijkl \rangle} \hat{\mathbf{S}}_{i'} \cdot \hat{\mathbf{S}}_{j'} + 4(\hat{Q}_{ijkl} + \hat{Q}_{iljk} - \hat{Q}_{ikjl}), \quad (\text{B1})$$

where

$$\hat{Q}_{ijkl} = (\hat{\mathbf{S}}_i \cdot \hat{\mathbf{S}}_j)(\hat{\mathbf{S}}_k \cdot \hat{\mathbf{S}}_l). \quad (\text{B2})$$

If the sum over all plaquettes  $\sum_{\langle ijkl \rangle}$  is performed, the first term (multiplied by  $J_c$ ) results in

$$J_c \sum_{\langle ijkl \rangle} \frac{1}{4} = \frac{3J_c}{4}L, \quad (\text{B3})$$

because there exist  $3L$  plaquettes for the  $L$ -site system under periodic-boundary conditions (see Fig. 1). Similarly, the second term results in

$$J_c \sum_{\langle ijkl \rangle} \sum_{i' < j' \in \langle ijkl \rangle} \hat{\mathbf{S}}_{i'} \cdot \hat{\mathbf{S}}_{j'} = 5J_c \sum_{\langle ij \rangle} \hat{\mathbf{S}}_i \cdot \hat{\mathbf{S}}_j + J_c \sum_{\langle\langle ij \rangle\rangle} \hat{\mathbf{S}}_i \cdot \hat{\mathbf{S}}_j, \quad (\text{B4})$$

where  $\langle\langle ij \rangle\rangle$  denotes a pair of spins on the next-nearest-neighbor sites  $i$  and  $j$  on the triangular lattice. The factor 5 in the first term is because the nearest-neighbor bonds ( $(i', j') = \{(i, j), (j, k), (k, l), (l, i), (j, l)\}$ ) appear five times in the sum over the plaquettes for the ring-exchange term. Similarly, the factor 1 in the second term is because the next-nearest-neighbor bond ( $(i', j') = \{(i, k)\}$ ) appears once for each plaquette. Now the full Hamiltonian is written as

$$\hat{H} = (J + 5J_c) \sum_{\langle ij \rangle} \hat{\mathbf{S}}_i \cdot \hat{\mathbf{S}}_j + J_c \sum_{\langle\langle ij \rangle\rangle} \hat{\mathbf{S}}_i \cdot \hat{\mathbf{S}}_j + 4J_c \sum_{\langle ijkl \rangle} (\hat{Q}_{ijkl} + \hat{Q}_{iljk} - \hat{Q}_{ikjl}) + \frac{3J_c L}{4}. \quad (\text{B5})$$

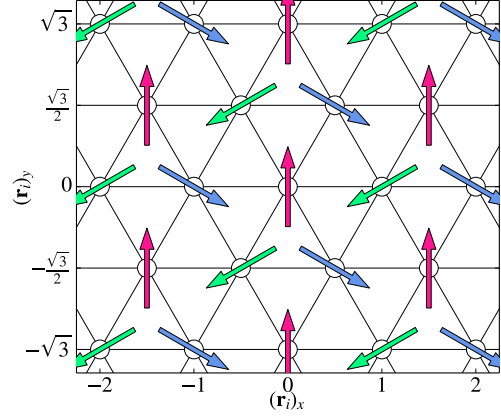


FIG. 7. Schematic figure of the  $120^\circ$  Néel state on the triangular lattice.  $(\mathbf{r}_i)_{x(y)}$  denotes the  $x$  ( $y$ ) coordinate of  $\mathbf{r}_i$ .

### 2. Rotating frame

The  $120^\circ$  Néel state has a three-sublattice structure, as shown in Fig. 7. However, introduction of the rotating frame [103–110] allows us to develop a one-sublattice spin-wave theory for the  $120^\circ$  Néel state.

In terms of the spin operators in the rotating frame ( $X$ - $Y$ - $Z$ ), the spin operators in the original frame ( $x$ - $y$ - $z$ ) can be written as

$$\begin{aligned} \hat{S}_i^x &= \cos \theta_i \hat{S}_i^X + \sin \theta_i \hat{S}_i^Z, \\ \hat{S}_i^y &= \hat{S}_i^Y, \\ \hat{S}_i^z &= \cos \theta_i \hat{S}_i^Z - \sin \theta_i \hat{S}_i^X, \end{aligned} \quad (\text{B6})$$

where  $\theta_i = \mathbf{Q} \cdot \mathbf{r}_i$  with  $\mathbf{Q} = (4\pi/3, 0)$  being a wave vector corresponding to the  $120^\circ$  order and  $\mathbf{r}_i$  the position of site  $i$ . The inner product of spin operators is thus given by

$$\begin{aligned} \hat{\mathbf{S}}_i \cdot \hat{\mathbf{S}}_j &= \hat{S}_i^Y \hat{S}_j^Y + (\hat{S}_i^Z \hat{S}_j^Z + \hat{S}_i^X \hat{S}_j^X) \cos \theta_{ij} \\ &\quad + (\hat{S}_i^Z \hat{S}_j^X - \hat{S}_i^X \hat{S}_j^Z) \sin \theta_{ij}, \end{aligned} \quad (\text{B7})$$

where  $\theta_{ij} = \theta_i - \theta_j$ .

We assume that the spins are pointing along  $Z$  axis of the rotating ( $X$ - $Y$ - $Z$ ) frame. The Holstein-Primakoff transformation [111] for the spin operators in the rotating frame results in

$$\begin{aligned} \hat{S}_i^Z &= S - \hat{a}_i^\dagger \hat{a}_i, \\ \hat{S}_i^- &= \sqrt{2S} \hat{a}_i^\dagger \left(1 - \frac{\hat{a}_i^\dagger \hat{a}_i}{2S}\right)^{\frac{1}{2}}, \\ \hat{S}_i^+ &= \sqrt{2S} \left(1 - \frac{\hat{a}_i^\dagger \hat{a}_i}{2S}\right)^{\frac{1}{2}} \hat{a}_i, \end{aligned} \quad (\text{B8})$$

where  $\hat{S}_i^- = \hat{S}_i^X - i\hat{S}_i^Y$ ,  $\hat{S}_i^+ = (\hat{S}_i^-)^\dagger$ , and  $\hat{a}_i$  and  $\hat{a}_i^\dagger$  are bosonic annihilation and creation operators, respectively, satisfying the canonical commutation relations  $[\hat{a}_i, \hat{a}_j] = 0$  and  $[\hat{a}_i, \hat{a}_j^\dagger] = \delta_{ij}$ .

### 3. Linear spin-wave approximation

Up to the quadratic terms of the bosonic operators, the inner product of the spin operators is approximated as

$$\begin{aligned}\hat{\mathbf{S}}_i \cdot \hat{\mathbf{S}}_j &\approx S^2 + S \cos \theta_{ij} (\hat{a}_i^\dagger \hat{a}_i + \hat{a}_j^\dagger \hat{a}_j) \\ &+ \frac{S}{2} (\cos \theta_{ij} + 1) (\hat{a}_i^\dagger \hat{a}_j + \hat{a}_j^\dagger \hat{a}_i) \\ &+ \frac{S}{2} (\cos \theta_{ij} - 1) (\hat{a}_i^\dagger \hat{a}_j^\dagger + \hat{a}_j \hat{a}_i). \quad (\text{B9})\end{aligned}$$

Notice that  $\cos \theta_{ij} = -1/2$  for the nearest neighbors and  $\cos \theta_{ij} = 1$  for next-nearest neighbors.

Similarly,  $\hat{Q}_{ijkl}$  is approximated as

$$\begin{aligned}\hat{Q}_{ijkl} &\approx \hat{S}_i^Z \hat{S}_j^Z \hat{S}_k^Z \hat{S}_l^Z \cos \theta_{ij} \cos \theta_{kl} \\ &+ \hat{S}_i^Z \hat{S}_j^Z \hat{S}_k^X \hat{S}_l^X \cos \theta_{ij} \cos \theta_{kl} \\ &+ \hat{S}_k^Z \hat{S}_l^Z \hat{S}_i^X \hat{S}_j^X \cos \theta_{ij} \cos \theta_{kl} \\ &+ \hat{S}_i^Z \hat{S}_j^Z \hat{S}_k^Y \hat{S}_l^Y \cos \theta_{ij} \\ &+ \hat{S}_k^Z \hat{S}_l^Z \hat{S}_i^Y \hat{S}_j^Y \cos \theta_{kl} \\ &+ (\hat{S}_i^Z \hat{S}_j^X - \hat{S}_i^X \hat{S}_j^Z) (\hat{S}_k^Z \hat{S}_l^X - \hat{S}_k^X \hat{S}_l^Z) \sin \theta_{ij} \sin \theta_{kl} \\ &\approx [S^4 - S^3 (\hat{a}_i^\dagger \hat{a}_i + \hat{a}_j^\dagger \hat{a}_j + \hat{a}_k^\dagger \hat{a}_k + \hat{a}_l^\dagger \hat{a}_l)] \cos \theta_{ij} \cos \theta_{kl} \\ &+ \frac{S^3}{2} (\hat{a}_i^\dagger \hat{a}_j + \text{H.c.}) \cos \theta_{kl} (\cos \theta_{ij} + 1) \\ &+ \frac{S^3}{2} (\hat{a}_k^\dagger \hat{a}_l + \text{H.c.}) \cos \theta_{ij} (\cos \theta_{kl} + 1) \\ &+ \frac{S^3}{2} (\hat{a}_i^\dagger \hat{a}_j^\dagger + \text{H.c.}) \cos \theta_{kl} (\cos \theta_{ij} - 1) \\ &+ \frac{S^3}{2} (\hat{a}_k^\dagger \hat{a}_l^\dagger + \text{H.c.}) \cos \theta_{ij} (\cos \theta_{kl} - 1) \\ &+ \frac{S^3}{2} \sin \theta_{ij} \sin \theta_{kl} \\ &\times (\hat{a}_j^\dagger \hat{a}_l - \hat{a}_j \hat{a}_l - \hat{a}_i^\dagger \hat{a}_l + \hat{a}_i \hat{a}_l + \\ &\hat{a}_j^\dagger \hat{a}_l^\dagger - \hat{a}_j \hat{a}_l^\dagger - \hat{a}_i^\dagger \hat{a}_k^\dagger + \hat{a}_i \hat{a}_k^\dagger + \text{H.c.}). \quad (\text{B10})\end{aligned}$$

By substituting  $\cos \theta_{ij} = \cos \theta_{kl} = \cos \theta_{il} = \cos \theta_{jk} = \cos \theta_{jl} = -1/2$ ,  $\cos \theta_{ik} = 1$ ,  $\sin \theta_{ij} \sin \theta_{kl} = -3/4$ ,  $\sin \theta_{il} \sin \theta_{jk} = 3/4$ , and  $\sin \theta_{ik} \sin \theta_{jl} = 0$  for  $\hat{Q}_{ijkl}$ ,  $\hat{Q}_{iljk}$ , and  $\hat{Q}_{ikjl}$ , we find

$$\begin{aligned}\hat{Q}_{ijkl} + \hat{Q}_{iljk} - \hat{Q}_{ikjl} \\ \approx S^4 - S^3 (\hat{a}_i^\dagger \hat{a}_i + \hat{a}_j^\dagger \hat{a}_j + \hat{a}_k^\dagger \hat{a}_k + \hat{a}_l^\dagger \hat{a}_l) \\ + \frac{S^3}{4} (\hat{a}_i^\dagger \hat{a}_j + \hat{a}_k^\dagger \hat{a}_l + \hat{a}_i^\dagger \hat{a}_l + \hat{a}_j^\dagger \hat{a}_k - \hat{a}_i^\dagger \hat{a}_k - 4\hat{a}_j^\dagger \hat{a}_l + \text{H.c.}) \\ + \frac{3S^3}{4} (\hat{a}_i^\dagger \hat{a}_j^\dagger + \hat{a}_k^\dagger \hat{a}_l^\dagger + \hat{a}_i^\dagger \hat{a}_l^\dagger + \hat{a}_j^\dagger \hat{a}_k^\dagger - \hat{a}_i^\dagger \hat{a}_k^\dagger + \text{H.c.}). \quad (\text{B11})\end{aligned}$$

Notice in Eq. (B11) that the subscript pair  $(i, k)$  contributes to the next-nearest-neighbor terms, while the others to the nearest-neighbor terms.

### 4. Spin-wave Hamiltonian

By substituting the approximations in Eqs. (B9) and (B11) into the Hamiltonian Eq. (B5), and carefully evaluating the sum over all plaquettes, similarly in Eq. (B4), we obtain the spin-wave Hamiltonian

$$\begin{aligned}\hat{H} \approx \hat{H}_{\text{sw}} = E_{\text{sw}} + 3S A_0 \sum_i \hat{a}_i^\dagger \hat{a}_i \\ + \frac{S}{4} \left[ A_1 \sum_{\langle ij \rangle} (\hat{a}_i^\dagger \hat{a}_j + \hat{a}_j^\dagger \hat{a}_i) + A_2 \sum_{\langle\langle ij \rangle\rangle} (\hat{a}_i^\dagger \hat{a}_j + \hat{a}_j^\dagger \hat{a}_i) \right] \\ - \frac{3S}{4} \left[ B_1 \sum_{\langle ij \rangle} (\hat{a}_i^\dagger \hat{a}_j^\dagger + \hat{a}_i \hat{a}_j) + B_2 \sum_{\langle\langle ij \rangle\rangle} (\hat{a}_i^\dagger \hat{a}_j^\dagger + \hat{a}_i \hat{a}_j) \right] \quad (\text{B12})\end{aligned}$$

where

$$\begin{aligned}A_0 &= J + 3J_c - 16S^2 J_c, \\ A_1 &= J + 5J_c, \\ A_2 &= 4(1 - S^2)J_c, \\ B_1 &= J + 5J_c - 16S^2 J_c, \\ B_2 &= 4S^2 J_c, \quad (\text{B13})\end{aligned}$$

and

$$E_{\text{sw}} = -\frac{3}{2} \left[ (J + 3J_c - 8S^2 J_c) S^2 - \frac{J_c}{2} \right] L. \quad (\text{B14})$$

With the Fourier transformation of the bosonic operators  $\hat{a}_i = \frac{1}{\sqrt{L}} \sum_{\mathbf{q}} \hat{a}_{\mathbf{q}} e^{i\mathbf{q} \cdot \mathbf{r}_i}$ ,  $\hat{H}_{\text{sw}}$  in the momentum space is given by

$$\begin{aligned}\hat{H}_{\text{sw}} &= E_{\text{sw}} + \sum_{\mathbf{q}} \left[ A(\mathbf{q}) \hat{a}_{\mathbf{q}}^\dagger \hat{a}_{\mathbf{q}} - \frac{1}{2} B(\mathbf{q}) (\hat{a}_{\mathbf{q}}^\dagger \hat{a}_{-\mathbf{q}}^\dagger + \hat{a}_{-\mathbf{q}} \hat{a}_{\mathbf{q}}) \right] \\ &= E_{\text{sw}} - \frac{1}{2} \sum_{\mathbf{q}} A(\mathbf{q}) \\ &+ \frac{1}{2} \sum_{\mathbf{q}} \begin{pmatrix} \hat{a}_{\mathbf{q}}^\dagger & \hat{a}_{-\mathbf{q}} \end{pmatrix} \begin{pmatrix} A(\mathbf{q}) & -B(\mathbf{q}) \\ -B(\mathbf{q}) & A(\mathbf{q}) \end{pmatrix} \begin{pmatrix} \hat{a}_{\mathbf{q}} \\ \hat{a}_{-\mathbf{q}}^\dagger \end{pmatrix}, \quad (\text{B15})\end{aligned}$$

where

$$A(\mathbf{q}) = 3S \left[ A_0 + \frac{A_1}{2} \gamma(\mathbf{q}) + \frac{A_2}{2} \gamma'(\mathbf{q}) \right], \quad (\text{B16})$$

$$B(\mathbf{q}) = \frac{9S}{2} [B_1 \gamma(\mathbf{q}) + B_2 \gamma'(\mathbf{q})], \quad (\text{B17})$$

$\gamma(\mathbf{q}) = \frac{1}{6} \sum_{i=1}^6 e^{i\mathbf{q} \cdot \delta_i}$ , and  $\gamma'(\mathbf{q}) = \frac{1}{6} \sum_{i=1}^6 e^{i\mathbf{q} \cdot \delta'_i}$  with  $\delta_i$  ( $\delta'_i$ ) being the vectors connecting the nearest (next-nearest) neighbors.

### 5. Spin-wave dispersion

We now introduce a Bogoliubov transformation

$$\begin{pmatrix} \hat{a}_{\mathbf{q}} \\ \hat{a}_{-\mathbf{q}}^\dagger \end{pmatrix} = \begin{pmatrix} u_{\mathbf{q}} & v_{\mathbf{q}} \\ v_{\mathbf{q}} & u_{\mathbf{q}} \end{pmatrix} \begin{pmatrix} \hat{b}_{\mathbf{q}} \\ \hat{b}_{-\mathbf{q}}^\dagger \end{pmatrix} \quad (\text{B18})$$

under the condition  $u_{\mathbf{q}}^2 - v_{\mathbf{q}}^2 = 1$  and thus the new operators  $\hat{b}_{\mathbf{q}}$  and  $\hat{b}_{\mathbf{q}}^\dagger$  obey the canonical bosonic commutation relations.

If  $u_{\mathbf{q}}$  and  $v_{\mathbf{q}}$  are chosen to satisfy  $u_{\mathbf{q}}^2 + v_{\mathbf{q}}^2 = A(\mathbf{q})/\Omega(\mathbf{q})$  and  $2u_{\mathbf{q}}v_{\mathbf{q}} = B(\mathbf{q})/\Omega(\mathbf{q})$  with

$$\Omega(\mathbf{q}) = \sqrt{A(\mathbf{q})^2 - B(\mathbf{q})^2}, \quad (\text{B19})$$

the spin-wave Hamiltonian is given by

$$\hat{H}_{\text{sw}} = E_{\text{sw}} - \frac{1}{2} \sum_{\mathbf{q}} A(\mathbf{q}) + \sum_{\mathbf{q}} \Omega(\mathbf{q}) \left( \hat{b}_{\mathbf{q}}^\dagger \hat{b}_{\mathbf{q}} + \frac{1}{2} \right), \quad (\text{B20})$$

where  $\Omega(\mathbf{q})$  is the spin-wave dispersion.

Figure 8(a) shows the  $S = 1/2$  spin-wave dispersion  $\Omega(\mathbf{q})$  for several values of  $J_c/J$  along the high symmetric momentum direction  $\Gamma$ - $K$ - $M$ - $\Gamma$ , where  $\Gamma = (0, 0)$ ,  $K = (4\pi/3, 0)$ , and  $M = (\pi, \pi/\sqrt{3})$ . The zero modes at the  $\Gamma$ ,  $K$ , and  $K'$  points are preserved because  $A(\Gamma) = B(\Gamma) = \frac{9S}{2} (J + 5J_c - 12S^2 J_c)$  and  $A(\pm K) = -B(\pm K) = \frac{9S}{4} (J + 5J_c - 24S^2 J_c)$ . The excitation energy at the  $M$  point is given by

$$\begin{aligned} \Omega(M) &= 2S \sqrt{[J - (3 + 28S^2)J_c][J + (3 - 16S^2)J_c]} \\ &= \sqrt{(J - 10J_c)(J - J_c)}, \end{aligned} \quad (\text{B21})$$

where the second line is for  $S = 1/2$ . It is found that the spin-wave excitation energy along the  $K$ - $M$  line, especially at the  $M$  point, reduces drastically with increasing  $J_c/J$ , and finally becomes zero when  $J_c/J = 0.1$ , implying instability of the  $120^\circ$  Néel order. On the other hand, the spin-wave velocity around the  $\Gamma$  point remains the same and the highest spin-wave excitation energy is kept around  $1.5J$  as  $J_c/J$  is increased.

For a comparison, Fig. 8(b) shows the  $S = 1/2$  linear spin-wave dispersion  $\Omega(\mathbf{q})$  for the  $J$ - $J'$  model defined as

$$\hat{H}_{JJ'} = J \sum_{\langle ij \rangle} \hat{\mathbf{S}}_i \cdot \hat{\mathbf{S}}_j + J' \sum_{\langle\langle ij \rangle\rangle} \hat{\mathbf{S}}_i \cdot \hat{\mathbf{S}}_j \quad (\text{B22})$$

with  $J'$  being the next-nearest-neighbor exchange interaction. The linear spin-wave dispersion for this model can be obtained by replacing  $A_0, A_1, A_2, B_1$ , and  $B_2$  in Eqs. (B16) and (B17) with  $\tilde{A}_0, \tilde{A}_1, \tilde{A}_2, \tilde{B}_1$ , and  $\tilde{B}_2$ , where

$$\begin{aligned} \tilde{A}_0 &= J - 2J', \\ \tilde{A}_1 &= J, \\ \tilde{A}_2 &= 4J', \\ \tilde{B}_1 &= J, \\ \tilde{B}_2 &= 0. \end{aligned} \quad (\text{B23})$$

Again the zero modes at the  $\Gamma$ ,  $K$ , and  $K'$  points are preserved with increasing  $J'/J$ . The excitation energy at the  $M$  point is given by

$$\begin{aligned} \Omega(M) &= 2S \sqrt{(J - 8J')(J - 2J')} \\ &= \sqrt{(J - 8J')(J - 2J')}. \end{aligned} \quad (\text{B24})$$

Similarly to the  $J$ - $J_c$  model, the spin-wave excitation energy at the  $M$  point reduces most significantly with increasing  $J'/J$ , and finally becomes zero when  $J'/J = 1/8$ . However, differently from the  $J$ - $J_c$  model, the spin-wave velocity around the

$\Gamma$  point reduces and the highest spin-wave excitation energy is

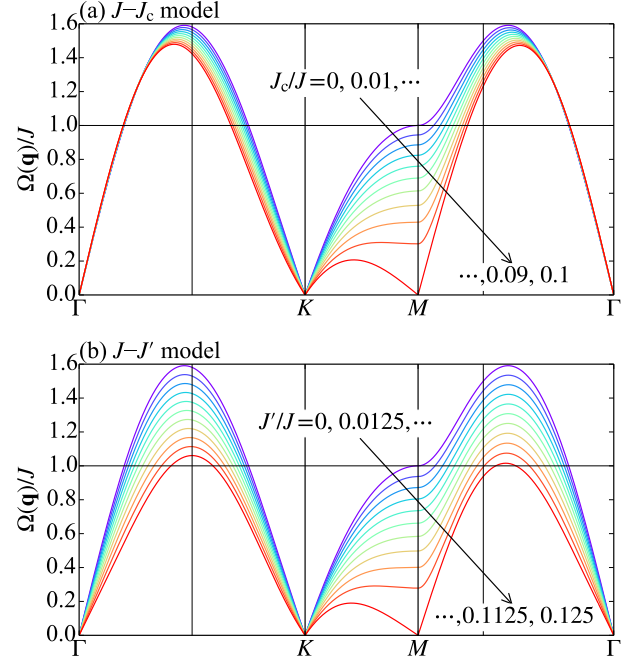


FIG. 8. Linear spin-wave dispersion for (a) the  $J$ - $J_c$  model and (b) the  $J$ - $J'$  model with several  $J_c/J$  and  $J'/J$  values indicated respectively in the figure. The horizontal axis is momentum  $\mathbf{q}$  along the  $\Gamma$ - $K$ - $M$ - $\Gamma$  points in the (non-magnetic) Brillouin zone, where  $\Gamma = (0, 0)$ ,  $K = (4\pi/3, 0)$ , and  $M = (\pi, \pi/\sqrt{3})$ . Thin vertical lines indicate the magnetic Brillouin-zone boundaries corresponding to the  $120^\circ$  Néel order. The horizontal line at  $\Omega(\mathbf{q})/J = 1$  indicates the spin-wave excitation energy at  $M$  point in the purely triangular case with  $J_c = J' = 0$ .

also reduced from  $\sim 1.6J$  to  $\sim 1.05J$  as  $J'/J$  is increased. A similar dependence of the excitation energy on the interaction parameter  $J'$  has been found also in the square lattice with the linear spin-wave theory [40].

The spin-wave excitation has two characteristic energy scales. One is the maxima of  $\Omega(\mathbf{q})$  and the other is the saddle points, minima, and nearly flat dispersion of  $\Omega(\mathbf{q})$  at and around the  $M$  and equivalent points. The comparison of the spin-wave dispersions suggests that, although both  $J_c$  and  $J'$  can increase the separation of the two energy scales, the more significant separation may appear in the  $J$ - $J_c$  model than in the  $J$ - $J'$  model. Note however that analytical and numerical studies beyond the linear spin-wave theory [13, 112, 113] have shown a strong renormalization of the magnon excitation energy as compared to the spin-wave theory for the pure triangular-lattice case with  $J_c = J' = 0$ .

Finally, we note that the spin-wave analysis captures the magnon excitations but not non-magnetic ones. Indeed, we were not able to find the double-peak structure of the specific heat within the spin-wave analysis. This implies that the non-magnetic excitations beyond the simple magnon excitations might be essential to understand the characteristic double-peak structure of the specific heat found here in the finite-temperature Lanczos calculations.



- 
- [1] P. Anderson, *Materials Research Bulletin* **8**, 153 (1973).
- [2] P. Fazekas and P. W. Anderson, *The Philosophical Magazine: A Journal of Theoretical Experimental and Applied Physics* **30**, 423 (1974).
- [3] B. Bernu, C. Lhuillier, and L. Pierre, *Phys. Rev. Lett.* **69**, 2590 (1992).
- [4] B. Bernu, P. Lecheminant, C. Lhuillier, and L. Pierre, *Phys. Rev. B* **50**, 10048 (1994).
- [5] G. Misguich, C. Lhuillier, B. Bernu, and C. Waldtmann, *Phys. Rev. B* **60**, 1064 (1999).
- [6] L. Capriotti, A. E. Trumper, and S. Sorella, *Phys. Rev. Lett.* **82**, 3899 (1999).
- [7] S. Yunoki and S. Sorella, *Phys. Rev. B* **74**, 014408 (2006).
- [8] S. R. White and A. L. Chernyshev, *Phys. Rev. Lett.* **99**, 127004 (2007).
- [9] P. Lecheminant, B. Bernu, C. Lhuillier, and L. Pierre, *Phys. Rev. B* **52**, 6647 (1995).
- [10] L. O. Manuel and H. A. Ceccatto, *Phys. Rev. B* **60**, 9489 (1999).
- [11] R. Kaneko, S. Morita, and M. Imada, *J. Phys. Soc. Jpn.* **83**, 093707 (2014).
- [12] Y. Iqbal, W.-J. Hu, R. Thomale, D. Poilblanc, and F. Becca, *Phys. Rev. B* **93**, 144411 (2016).
- [13] F. Ferrari and F. Becca, *Phys. Rev. X* **9**, 031026 (2019).
- [14] O. I. Motrunich, *Phys. Rev. B* **72**, 045105 (2005).
- [15] R. V. Mishmash, J. R. Garrison, S. Bieri, and C. Xu, *Phys. Rev. Lett.* **111**, 157203 (2013).
- [16] C. J. Calzado and J.-P. Malrieu, *Phys. Rev. B* **69**, 094435 (2004).
- [17] K. Tanaka, Y. Yokoyama, and C. Hotta, *J. Phys. Soc. Jpn.* **87**, 023702 (2018).
- [18] H. Morita, S. Watanabe, and M. Imada, *J. Phys. Soc. Jpn.* **71**, 2109 (2002).
- [19] T. Koretsune, Y. Motome, and A. Furusaki, *Journal of the Physical Society of Japan* **76**, 074719 (2007).
- [20] P. Sahebsara and D. Sénéchal, *Phys. Rev. Lett.* **100**, 136402 (2008).
- [21] T. Yoshioka, A. Koga, and N. Kawakami, *Phys. Rev. Lett.* **103**, 036401 (2009).
- [22] L. F. Tocchio, H. Feldner, F. Becca, R. Valentí, and C. Gros, *Phys. Rev. B* **87**, 035143 (2013).
- [23] A. Yamada, *Phys. Rev. B* **89**, 195108 (2014).
- [24] M. Laubach, R. Thomale, C. Platt, W. Hanke, and G. Li, *Phys. Rev. B* **91**, 245125 (2015).
- [25] K. Misumi, T. Kaneko, and Y. Ohta, *Phys. Rev. B* **95**, 075124 (2017).
- [26] T. Shirakawa, T. Tohyama, J. Kokalj, S. Sota, and S. Yunoki, *Phys. Rev. B* **96**, 205130 (2017).
- [27] J. Skolimowski, Y. Gerasimenko, and R. Žitko, *Phys. Rev. Lett.* **122**, 036802 (2019).
- [28] A. K. McMahan and J. W. Wilkins, *Phys. Rev. Lett.* **35**, 376 (1975).
- [29] J. H. Hetherington and F. D. C. Willard, *Phys. Rev. Lett.* **35**, 1442 (1975).
- [30] M. Roger, J. M. Delrieu, and J. H. Hetherington, *Phys. Rev. Lett.* **45**, 137 (1980).
- [31] K. Yosida, *Progress of Theoretical Physics Supplement* **69**, 475 (1980).
- [32] D. M. Ceperley and G. Jacucci, *Phys. Rev. Lett.* **58**, 1648 (1987).
- [33] M. Roger, *Journal of Low Temperature Physics* **162**, 625 (2011).
- [34] L. Cândido, G.-Q. Hai, and D. M. Ceperley, *Phys. Rev. B* **84**, 064515 (2011).
- [35] K. Yosida and S. Inagaki, *J. Phys. Soc. Jpn.* **50**, 3268 (1981).
- [36] J. Lorenzana, J. Eroles, and S. Sorella, *Phys. Rev. Lett.* **83**, 5122 (1999).
- [37] R. Coldea, S. M. Hayden, G. Aeppli, T. G. Perring, C. D. Frost, T. E. Mason, S.-W. Cheong, and Z. Fisk, *Phys. Rev. Lett.* **86**, 5377 (2001).
- [38] A. A. Katanin and A. P. Kampf, *Phys. Rev. B* **66**, 100403 (2002).
- [39] N. S. Headings, S. M. Hayden, R. Coldea, and T. G. Perring, *Phys. Rev. Lett.* **105**, 247001 (2010).
- [40] M. S. Rutonjski, M. V. Pavkov-Hrvojević, and M. B. Berović, *International Journal of Modern Physics B* **30**, 1550251 (2016).
- [41] S. Yamamoto and Y. Noriki, *Phys. Rev. B* **99**, 094412 (2019).
- [42] K. T. Law and P. A. Lee, *Proceedings of the National Academy of Sciences* **114**, 6996 (2017).
- [43] W.-Y. He, X. Y. Xu, G. Chen, K. T. Law, and P. A. Lee, *Phys. Rev. Lett.* **121**, 046401 (2018).
- [44] Y. Shimizu, K. Miyagawa, K. Kanoda, M. Maesato, and G. Saito, *Phys. Rev. Lett.* **91**, 107001 (2003).
- [45] Y. Kurosaki, Y. Shimizu, K. Miyagawa, K. Kanoda, and G. Saito, *Phys. Rev. Lett.* **95**, 177001 (2005).
- [46] R. S. Manna, M. de Souza, A. Brühl, J. A. Schlueter, and M. Lang, *Phys. Rev. Lett.* **104**, 016403 (2010).
- [47] T. Itou, A. Oyamada, S. Maegawa, M. Tamura, and R. Kato, *Phys. Rev. B* **77**, 104413 (2008).
- [48] M. Yamashita, N. Nakata, Y. Senshu, M. Nagata, H. M. Yamamoto, R. Kato, T. Shibauchi, and Y. Matsuda, *Science* **328**, 1246 (2010).
- [49] P. Fazekas and E. Tosatti, *Philosophical Magazine B* **39**, 229 (1979).
- [50] M. Klanjšek, A. Zorko, R. Zitko, J. Mravlje, Z. Jagličić, P. Biswas, P. Prelovsek, D. Mihailović, and D. Arcon, *Nature Physics* **13**, 1130 (2017), article.
- [51] M. Roger, *Phys. Rev. B* **30**, 6432 (1984).
- [52] M. Roger, *Phys. Rev. Lett.* **64**, 297 (1990).
- [53] K. Ishida, M. Morishita, K. Yawata, and H. Fukuyama, *Phys. Rev. Lett.* **79**, 3451 (1997).
- [54] M. Roger, C. Bäuerle, Y. M. Bunkov, A.-S. Chen, and H. Godfrin, *Phys. Rev. Lett.* **80**, 1308 (1998).
- [55] H. Fukuyama, *J. Phys. Soc. Jpn.* **77**, 111013 (2008).
- [56] T. Momoi, H. Sakamoto, and K. Kubo, *Phys. Rev. B* **59**, 9491 (1999).
- [57] T. Momoi, P. Sindzingre, and N. Shannon, *Phys. Rev. Lett.* **97**, 257204 (2006).
- [58] T. Momoi, P. Sindzingre, and K. Kubo, *Phys. Rev. Lett.* **108**, 057206 (2012).
- [59] Y. Fuseya and M. Ogata, *J. Phys. Soc. Jpn.* **78**, 013601 (2009).
- [60] K. Seki, T. Shirakawa, and Y. Ohta, *Phys. Rev. B* **79**, 024303 (2009).
- [61] S. Moroni and M. Boninsegni, *Phys. Rev. B* **99**, 195441 (2019).
- [62] W. LiMing, G. Misguich, P. Sindzingre, and C. Lhuillier, *Phys. Rev. B* **62**, 6372 (2000).
- [63] R. Kato, *Bulletin of the Chemical Society of Japan* **87**, 355 (2014).
- [64] R. Rawl, L. Ge, H. Agrawal, Y. Kamiya, C. R. Dela Cruz, N. P. Butch, X. F. Sun, M. Lee, E. S. Choi, J. Oitmaa, C. D. Batista,

- M. Mourigal, H. D. Zhou, and J. Ma, *Phys. Rev. B* **95**, 060412 (2017).
- [65] Y. Cui, J. Dai, P. Zhou, P. S. Wang, T. R. Li, W. H. Song, J. C. Wang, L. Ma, Z. Zhang, S. Y. Li, G. M. Luke, B. Normand, T. Xiang, and W. Yu, *Phys. Rev. Materials* **2**, 044403 (2018).
- [66] P. Prelovšek, K. Morita, T. Tohyama, and J. Herbrych, [arXiv:1912.00876 \[cond-mat.str-el\]](https://arxiv.org/abs/1912.00876).
- [67] J. Jaklič and P. Prelovšek, *Phys. Rev. B* **49**, 5065 (1994).
- [68] J. Jaklič and P. Prelovšek, *Adv. Phys.* **49**, 1 (2000).
- [69] P. Prelovšek and J. Bonča, “Ground state and finite temperature lanczos methods,” in *Strongly Correlated Systems: Numerical Methods*, edited by A. Avella and F. Mancini (Springer Berlin Heidelberg, Berlin, Heidelberg, 2013) pp. 1–30.
- [70] T. Iitaka and T. Ebisuzaki, *Phys. Rev. E* **69**, 057701 (2004).
- [71] A. Weiße, G. Wellein, A. Alvermann, and H. Fehske, *Rev. Mod. Phys.* **78**, 275 (2006).
- [72] D. A. Drabold and O. F. Sankey, *Phys. Rev. Lett.* **70**, 3631 (1993).
- [73] F. Chatelin, *Valeurs propres de matrices* (Masson, Paris, 1988) translation by M. Iri and Y. Iri (Springer, Tokyo, 2003).
- [74] T. Shirakawa and S. Yunoki, *Phys. Rev. B* **90**, 195109 (2014).
- [75] A. Allerd, C. A. Büsler, G. B. Martins, and A. E. Feiguin, *Phys. Rev. B* **91**, 085101 (2015).
- [76] K. Seki, T. Shirakawa, and S. Yunoki, *Phys. Rev. B* **98**, 205114 (2018).
- [77] M. Aichhorn, M. Daghofer, H. G. Evertz, and W. von der Linden, *Phys. Rev. B* **67**, 161103 (2003).
- [78] J. Schnack, J. Schulenburg, and J. Richter, *Phys. Rev. B* **98**, 094423 (2018).
- [79] S. Sugiura and A. Shimizu, *Phys. Rev. Lett.* **111**, 010401 (2013).
- [80] H. Nishida, R. Fujiuchi, K. Sugimoto, and Y. Ohta, (2019), [arXiv:1909.09335 \[cond-mat.str-el\]](https://arxiv.org/abs/1909.09335).
- [81] H. Tal-Ezer and R. Kosloff, *The Journal of Chemical Physics* **81**, 3967 (1984).
- [82] L.-W. Wang, *Phys. Rev. B* **49**, 10154 (1994).
- [83] L.-W. Wang and A. Zunger, *Phys. Rev. Lett.* **73**, 1039 (1994).
- [84] T. Iitaka, *Phys. Rev. E* **49**, 4684 (1994).
- [85] A. Vijay and H. Metiu, *The Journal of Chemical Physics* **116**, 60 (2002).
- [86] T. Iitaka and T. Ebisuzaki, *Phys. Rev. Lett.* **90**, 047203 (2003).
- [87] M. Machida, T. Iitaka, and S. Miyashita, *J. Phys. Soc. Jpn.* **74**, 107 (2005).
- [88] A. Weiße and H. Fehske, *Computational Many-Particle Physics*, edited by H. Fehske, R. Schneider, and A. Weiße, Lect. Notes Phys. 739 (Springer, Berlin Heidelberg, 2008) Chap. 19, pp. 545–577.
- [89] K. Seki, Y. Otsuka, S. Yunoki, and S. Sorella, *Phys. Rev. B* **99**, 125145 (2019).
- [90] J. M. Deutsch, *Phys. Rev. A* **43**, 2046 (1991).
- [91] M. Srednicki, *Phys. Rev. E* **50**, 888 (1994).
- [92] I. Rousochatzakis, S. Kourtis, J. Knolle, R. Moessner, and N. B. Perkins, *Phys. Rev. B* **100**, 045117 (2019).
- [93] P. Prelovšek and J. Kokalj, [arXiv:1906.11576](https://arxiv.org/abs/1906.11576).
- [94] P. Prelovšek and J. Kokalj, *Phys. Rev. B* **98**, 035107 (2018).
- [95] B.-B. Chen, L. Chen, Z. Chen, W. Li, and A. Weichselbaum, *Phys. Rev. X* **8**, 031082 (2018).
- [96] L. Chen, D.-W. Qu, H. Li, B.-B. Chen, S.-S. Gong, J. von Delft, A. Weichselbaum, and W. Li, *Phys. Rev. B* **99**, 140404 (2019).
- [97] P. Lecheminant, B. Bernu, C. Lhuillier, L. Pierre, and P. Sindzingre, *Phys. Rev. B* **56**, 2521 (1997).
- [98] Waltdmann, Ch., Everts, H.-U., Bernu, B., Lhuillier, C., Sindzingre, P., Lecheminant, P., and Pierre, L., *Eur. Phys. J. B* **2**, 501 (1998).
- [99] T. Shimokawa and H. Kawamura, *J. Phys. Soc. Jpn.* **85**, 113702 (2016).
- [100] Y. Yamaji, T. Suzuki, T. Yamada, S.-i. Suga, N. Kawashima, and M. Imada, *Phys. Rev. B* **93**, 174425 (2016).
- [101] N. D. Mermin and H. Wagner, *Phys. Rev. Lett.* **17**, 1133 (1966).
- [102] H. Q. Lin, *Phys. Rev. B* **42**, 6561 (1990).
- [103] T. Oguchi, H. Nishimori, and Y. Taguchi, *J. Phys. Soc. Jpn.* **54**, 4494 (1985).
- [104] S. J. Miyake, *Progress of Theoretical Physics* **74**, 468 (1985).
- [105] P. W. Leung and K. J. Runge, *Phys. Rev. B* **47**, 5861 (1993).
- [106] T. Ohyama and H. Shiba, *J. Phys. Soc. Jpn.* **62**, 3277 (1993).
- [107] R. Deutscher and H. U. Everts, *Zeitschrift für Physik B Condensed Matter* **93**, 77 (1993).
- [108] A. E. Trumper, L. Capriotti, and S. Sorella, *Phys. Rev. B* **61**, 11529 (2000).
- [109] A. L. Chernyshev and M. E. Zhitomirsky, *Phys. Rev. B* **79**, 144416 (2009).
- [110] M. E. Zhitomirsky and A. L. Chernyshev, *Rev. Mod. Phys.* **85**, 219 (2013).
- [111] T. Holstein and H. Primakoff, *Phys. Rev.* **58**, 1098 (1940).
- [112] W. Zheng, J. O. Fjærestad, R. R. P. Singh, R. H. McKenzie, and R. Coldea, *Phys. Rev. B* **74**, 224420 (2006).
- [113] E. A. Ghioldi, A. Mezio, L. O. Manuel, R. R. P. Singh, J. Oitmaa, and A. E. Trumper, *Phys. Rev. B* **91**, 134423 (2015).